

Jurassic Hornblende Gabbros in Dongga, Eastern Gangdese, Tibet: Partial Melting of Mantle Wedge and Implications for Crustal Growth

XU Bo^{1,2}, HOU Zengqian^{2,*}, ZHENG Yuanchuan¹, ZHOU Ye², ZHOU Limin³, YANG Yu⁴,
HAN Yanwei⁵, ZHEN Guo⁶ and WU Changda¹

¹ School of Earth Science and Mineral Resources, China University of Geosciences, Beijing 10083, China

² Institute of Geology, Chinese Academy of Geological Sciences, Beijing 100037, China

³ National Research Center for Geoanalysis, Chinese Academy of Geological Sciences, Beijing 100037, China

⁴ State Key Laboratory of Earthquake Dynamics, Institute of Geology, China Earthquake Administration, Beijing 100029, China

⁵ Kunming Foundation Engineering Company of China Nonferrous Metals Industry, Kunming 654000, China

⁶ Department of Ocean Science and Engineering, South University of Science and Technology of China, Shenzhen, 518055 China

Abstract: The Gangdese batholith, more than 2500 km in length, is composed mainly of Jurassic-Miocene igneous rocks. This batholith is one of the most important constituents of the Tibetan orogenesis and provides an ideal place for study of Neo-Tethyan ocean geodynamic evolution and plateau uplift. Recent studies on the Gangdese Jurassic felsic magmatism highlight its juvenile source. However, important aspects concerning the genesis of the juvenile magmatism and related deep geodynamic evolution are still unclear. Here, we report detailed petrological, geochronological, geochemical, whole-rock Sr-Nd isotopic, and in situ Sr-Hf isotopic data for a recently identified hornblende gabbro in the Dongga area, southern Lhasa sub-block. This hornblende gabbro is dominated by hornblende and plagioclase, dated at Early Jurassic (ca. 180–190 Ma), and characterized by a narrow compositional range in SiO₂ (49.38wt%–52.27wt%), MgO (4.08wt%–7.00wt%), FeO (10.43wt%–11.77wt%), Na₂O (2.58wt%–3.51wt%), and K₂O (0.48wt%–1.53wt%). It has depleted isotopic signatures, with whole-rock (⁸⁷Sr/⁸⁶Sr)_i ratios of 0.7033–0.7043, $\varepsilon_{\text{Nd}}(t)$ values of +4.90 to +6.99, in situ plagioclase (⁸⁷Sr/⁸⁶Sr)_i ratios of 0.7034–0.7042, and zircon $\varepsilon_{\text{Hf}}(t)$ of +12.2 to +16.8. Our results integrated with published data suggest a model of Gangdese juvenile crustal growth by a subduction-related water-enriched mantle wedge. The hydrous partial melting of the lithosphere mantle was triggered by the dehydration of a Neo-Tethyan oceanic slab. This mafic magmatism emplaced in the middle-lower crust of intraoceanic arcs or active continental margins, leading to Jurassic juvenile crustal growth in southern Tibet.

Key words: crustal growth, zircon U-Pb age, mantle, water-enriched, Gangdese belt, Tibet, Proto-Tethys

1 Introduction

The Tibetan plateau was assembled by the accretion of a number of Gondwana-derived terranes to Asia since the Early Paleozoic (Yin and Harrison, 2000; Chung et al., 2005). The northward subduction of the Neo-Tethyan oceanic lithosphere and the subsequent India-Asia continental collision along the Yarlung-Tsangpo suture developed this “Roof of the World.” The growth of the Tibetan plateau ultimately influences Asian monsoon

* Corresponding author. E-mail: houzengqian@126.com

intensity and even global climate (e.g., Molnar et al., 1993; An et al., 2001). Therefore, the knowledge of crustal uplift related to initial subduction of the Neo-Tethyan oceanic lithosphere is significant in understanding the initial growth mechanism of the plateau since the Jurassic (Ji et al., 2009; Chu et al., 2011; Guo et al., 2013; Wang et al., 2016, and references therein). An important issue is raised by the observation of Early Jurassic igneous rocks with high and positive $\varepsilon_{\text{Nd}}(t)$ (up to +7.5) and $\varepsilon_{\text{Hf}}(t)$ (up to +18) values (Ji et al., 2009; Chu et al., 2011; Yang et al., 2008, 2009, 2015; Hou et al., 2015, and references

therein). These indicate important mantle input in the Jurassic in the Lhasa block. However, the mechanisms for the generation of mantle-derived magma as well as the associated geodynamic processes in the crustal growth are still unclear. Exposures of contemporaneous mantle-derived mafic rocks in the Gangdese belt are therefore critically important because they record information regarding the chemical composition of the mantle, and their detailed examination will give information on the formation, evolution of the crustal growth, and the related geodynamic processes during the Neo-Tethyan oceanic lithosphere subduction in the Early Jurassic.

For better understanding the processes of Jurassic Tibetan mafic magmatism emplacement and the crustal growth mechanism, we present combined geological, whole-rock and mineral geochemical, and isotopic data for Jurassic Dongga hornblende gabbros. Our results indicate that this magmatism was derived from the water-enriched mantle wedge released by a subducting oceanic slab. Invasion of these mafic melts into the lower crust is key to the formation of the Jurassic felsic magmatism and crustal growth in southern Tibet.

2 Geologic Setting and Magmatism

2.1 Tectonic framework

The Tibetan Plateau is composed of four continental blocks: from north to south, they are the Songpan-Ganzi terrane, Qiangtang terrane, Lhasa terrane, and Himalayan sequences. These four blocks are separated by the Jinsha, Bangong-Nujiang, and Indus-Yarlung Zangbo suture zones, respectively (Yin and Harrison, 2000; Zhu et al., 2013). The Lhasa terrane represents the southernmost Asian block and is bounded by the Yarlung-Zangbo suture in the south and the Bangong-Nujiang suture in the north. The Lhasa terrane is subdivided into northern, central, and southern subterrane (Zhu et al., 2011; Xu et al., 2017) (Fig. 1a). The central subterrane consists of an Archean and Proterozoic crystalline basement, covered by Paleozoic and Mesozoic metasedimentary and volcanic rocks (Zhu et al., 2009, 2011). The southern and northern Lhasa subterrane are characterized by juvenile crust related to arc magmatism (Ji et al., 2009; Zhu et al., 2011; Chen Yanhong et al., 2015; Hou et al., 2004, 2015; Wang et al., 2015). The northward subduction of the Neo-Tethys oceanic lithosphere beneath the southern margin of the Lhasa terrane began in the Late Triassic or Early Jurassic and ended by the arrival of the Greater Indian continent in the Early Cenozoic (Ji et al., 2009; Zhu et al., 2011; Xiong et al., 2016). The convergence and subduction beneath the Lhasa block resulted in the formation of voluminous calc-alkaline granitoids in the 2500 km-long, east-to-west-

trending Gangdese belt (Zhang Hongfei et al., 2007; Wen Daren, 2007; Wu et al., 2010; Zhu et al., 2011, 2015; Chu et al., 2011; Ding et al., 2014 and references therein).

2.2 Magmatism

The Early Mesozoic igneous rocks in the Gangdese magmatic belt include Late Triassic-Early Jurassic calc-alkaline granitoid rocks (Chu et al., 2006; Guo et al., 2013; Hou et al., 2015, 2012; Ji et al., 2009; Wang et al., 2014a, 2014b, 2014c, 2015; Zheng et al., 2012, 2014), S-type granites in the Nyainqntanglha-Damxung area (Kapp et al., 2005; Pullen et al., 2008), and a suite of Jurassic volcanic rocks (Dong Yanhui et al., 2006; Kang Zhiqiang et al., 2009, 2010; Zhu et al., 2008; 2009; Lv et al., 2015). These less-exposed Jurassic granitoids and volcanic rocks form a 600-km-long Jurassic arc system (Geng Quanru et al., 2005), extending from Xietongmen to Milin along the north side of Yarlung-Zangbo River (Fig. 1a–b). According to distinct geochemical signatures, this Jurassic granitoid belt can be divided into two groups (Hou et al., 2015). The Jurassic intrusions include tonalites, granodiorites, monzogranites, and gabbros (Chu et al., 2006; Ji et al., 2009; Qu et al., 2007; Tang Juxing et al., 2010; Zhang Hongfei et al., 2007). Coeval Jurassic porphyry-type mineralization is found to be associated with the quartz diorite porphyry intrusions located in Gangdese belt (Hou et al., 2015) (e.g., Xiongcun, Laze, and Zemoduola). The Jurassic volcanic rocks are mainly composed of Yeba Formation volcanic rocks (175–190 Ma; Dong Yanhui et al., 2006; Zhu et al., 2008) and Sangri Group volcanics (145–195 Ma; Kang Zhiqiang et al., 2009, 2010; Zhu et al., 2009). The Yeba volcanic sequences are truncated by Late Cretaceous granites to the north and show fault-unconformable contact with Cretaceous volcanic rocks to the south (Fig. 1b; Dong Yanhui et al., 2006; Zhu et al., 2008). The Sangri Group is widely distributed in the central and eastern Gangdese belt between the towns of Saga in the west and Sangri in the east (Fig. 1b). These suites of volcanoes consist of basalt, basaltic andesite, andesite, and minor dacite, interbedded with sandstone, slate, and other sedimentary rocks (Kang et al., 2014; Zhu et al., 2009).

2.3 Sampling and petrology

This study focuses particularly on understanding the petrogenesis of the Dongga hornblende gabbros in southern Tibet. The Dongga Jurassic hornblende gabbros are located in southeastern Xietongmen county (Fig. 1c), surrounded by Eocene granites and few Jurassic granodiorites. Hornblende gabbros are fresh and do not show strong alteration under a microscope, as also attested by the low loss on ignition values. The rocks also do not exhibit

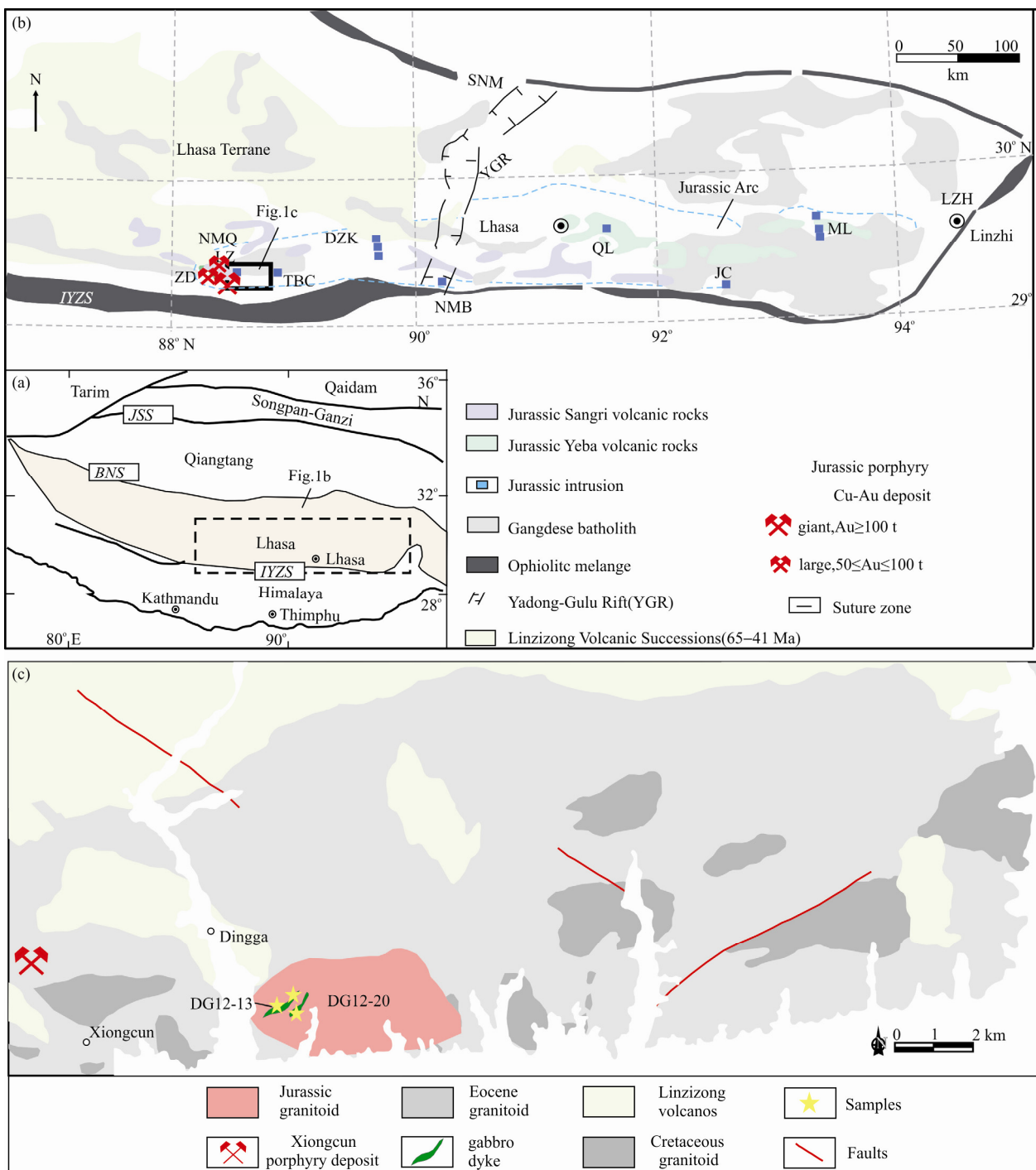


Fig. 1. (a) Tectonic framework of the Tibetan plateau (modified from Zhu et al., 2008). JSS, Jinsha suture; BNS, Bangonghu-Nujiang suture; IYZS, Indus-Yarlung Zangbo suture. (b) Geological map of the Lhasa terrane showing distribution of Jurassic magmatic rocks and associated porphyry Cu deposits. The Jurassic arc is delineated by outcrops of Jurassic intrusive and volcanic rocks.

Jurassic intrusive rocks: XC, Xiongcun; TBC, Tangbaicun; DZK, Dazhuka; NMB, Ni Mu Bridge; ML, Milin; NMQ, Nanmuqie; LZH, Linzhi. C: Simplified geological map and relative positions of the Xiongcun Cu–Au deposit and Jurassic plutons in the Xietongmen area, southern Tibet.

obvious structural deformation (Fig. 2a–h). The hornblende gabbros occur as dikes with ~0.5–2 m in diameter on outcrops and their thin sections show a coarse-medium grained igneous texture. They primarily consist of amphiboles (40%–50%) and plagioclases (35%–45%),

with a small amount of clinopyroxene (5%), magnetite, and accessory minerals (together ~ 5%). Euhedral plagioclase phenocrysts show multiple and polysynthetical twins and oscillatory zones. Several plagioclases cut across hornblende (Fig. 2c, e, g) and some plagioclases fill

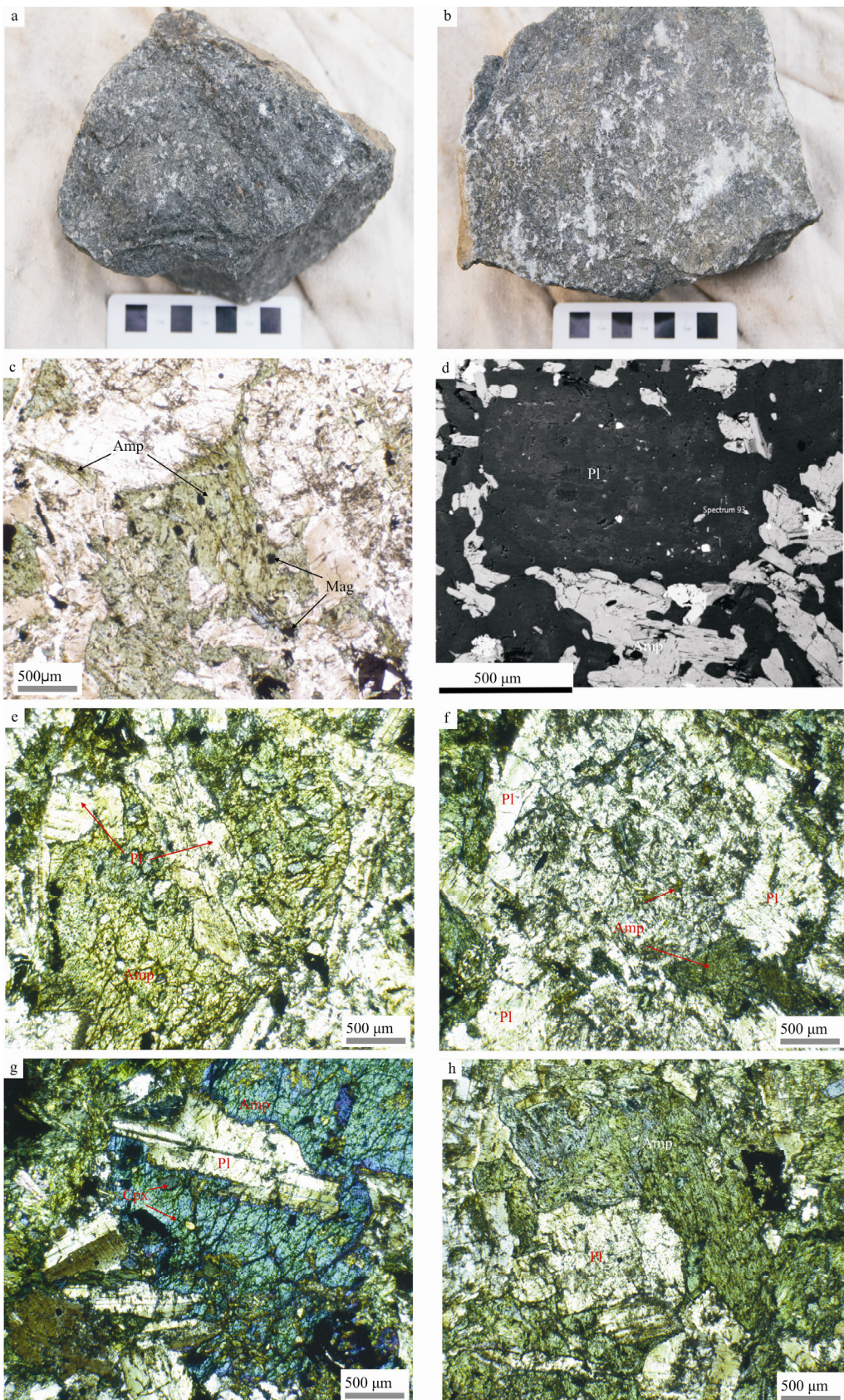


Fig. 2. Representative hand specimen photos and photomicrographs of the Dongga gabbros.

(a,b), Hand specimen; (c), Photomicrographs of the Dongga gabbros (sample DG12-05; plane-polarized light); (d), Representative BSE image of the hornblende gabbro; (e-h), Photomicrographs of the Dongga gabbros (samples DG12-13, DG12-14, and DG12-16; plane-polarized light). Abbreviations: Amp, Amphibole; Cpx, clinopyroxene; Mag, magnetite; Plg, plagioclase.

embayments in hornblende (Fig. 2b, h). Anhedral to subhedral amphiboles consist of green to greenish brown pleochroic grains. Amphiboles can be found with two types of crystals: tabular and acicular (Fig. 2b–c). Tabular crystals have long axes of up to 2–3 mm length (Fig. 2b–h) and acicular crystals vary from 100 micrometers to 0.5 millimeter in length (Fig. 2b, c). Some hornblende grains are enclosed within plagioclase (Fig. 2f). Some tabular hornblendes contain clinopyroxene (Fig. 2g). Therefore, on the basis of textural relationships, the mineral crystallization sequence may be summarized as (1) early-stage crystalizing minerals: clinopyroxene + anhedral to subhedral amphibole; (2) late-stage crystalizing minerals: subhedral plagioclase + biotite + epidote + magnetite.

In this study, five hornblende gabbros were selected for analysis of whole-rock major- and trace-element, Sr-Nd isotopic, and in situ plagioclase Sr isotopic data. Two samples were dated by zircon U-Pb dating. In situ Hf isotopic compositions of igneous zircons from the selected two samples were also analyzed to further differentiate crustal versus mantle contributions and to constrain magmatic evolution.

3 Analytical Methods

3.1 Mineral major-element analyses

Electron probe microanalysis was carried out at the Institute of Geology, Chinese Academy of Geological Sciences (CAGS), using a JEOL JXA-8800R electron microprobe. Selected representative minerals were analyzed using a 15 kV accelerating voltage, with 20 nA beam current of and 5 μm beam diameter. The counting times were 10 s for the peak and 5 s for background

measurements on each side of the peak. The results are listed in Table 1.

3.2 Whole-rock major- and trace-element geochemistry

Representative samples for major element oxides and trace elements are analyzed by X-ray fluorescence (XRF) and inductively coupled plasma mass spectrometry (ICP-MS) with an Agilent 7500ce instrument, respectively, at the Key Laboratory of Orogenic Belts and Crustal Evolution, Ministry of Education, Peking University (Table 2). The major elements of analytical uncertainties are less than 1% for the XRF analyses, and estimated from repeated analyses of two standards (andesite GSR-2 and basalt GSR-3). The uncertainties of the ICP-MS for trace elements measured are less than 5 % relatively.

3.3 LA-ICP-MS zircon U-Pb dating

Three samples were subjected to zircon U-Pb dating. Zircons were separated by heavy-liquid and magnetic methods and then purified by hand-picking under a binocular microscope. The extracted zircons were documented with transmitted- and reflected-light photomicrographs and cathodoluminescence (CL) images to reveal their internal information. Zircon U-Pb dating was conducted using laser ablation inductively coupled plasma mass spectrometry (LA-ICP-MS) at the Chinese Academy of Geological Science (CAGS), Beijing, following the procedures described by Hou et al. (2009). The spot size was 25 μm , the laser energy density, 2.5 J/cm², and the repetition rate, 10 Hz. The reference standards were GJ-1 zircon (age, 599.8±1.7 Ma (2r); Jackson et al., 2004) and Plesovice zircon (age, 337.13±0.37 (2r)). The GLITTER software (Griffin et al.,

Table 1 Representative compositions and the structural formula of the Dongga gabbro plagioclase phenocrysts

Samples	DGP05-1	DGP05-2	DGP05-3	DGP06-11	DGP06-12	DGP06-13	DGP019-1	DGP019-2	DGP019-3	DGP20-1	DGP20-2	DGP20-3
Position	Rim	Core	Core	Core	Core	Rim	Rim	Core	Core	Core	Rim	Rim
oxide (wt%)												
SiO ₂	58.104	57.597	58.265	58.259	58.335	58.585	58.155	58.803	58.193	57.516	56.296	57.282
TiO ₂	0	0	0	0	0	0	0	0	0	0	0	0
Al ₂ O ₃	27.208	27.43	26.882	26.139	26.056	26.16	26.261	26.841	26.98	26.916	27.626	27.06
FeO	0.059	0.136	0.101	0.222	0.102	0.164	0.136	0.074	0.06	0.125	0.126	0.123
MnO	0	0	0	0	0	0	0	0	0	0	0	0
MgO	0	0	0.007	0	0	0	0	0.003	0	0	0	0
CaO	9.411	9.549	8.921	8.4	8.158	8.417	8.418	8.383	9.058	9.153	9.642	9.588
Na ₂ O	6.939	6.769	7.182	7.331	7.466	7.172	7.264	7.558	7.137	6.915	6.689	6.55
K ₂ O	0.116	0.199	0.121	0.158	0.17	0.217	0.132	0.088	0.146	0.107	0.109	0.152
Total	101.837	101.68	101.479	100.509	100.287	100.715	100.366	101.75	101.574	100.732	100.488	100.755
Si	10.2591	10.1989	10.3157	10.4082	10.4344	10.4349	10.3970	10.3684	10.2971	10.2653	10.0970	10.2278
Ti	0.0000	0.0000	0.0000	0.0000	0.0000	0.0000	0.0000	0.0000	0.0000	0.0000	0.0000	0.0000
Al	5.6615	5.7241	5.6090	5.5034	5.4926	5.4912	5.5330	5.5775	5.6262	5.6614	5.8393	5.6940
Fe	0.0087	0.0201	0.0150	0.0332	0.0153	0.0244	0.0203	0.0109	0.0089	0.0187	0.0189	0.0184
Mn	0.0000	0.0000	0.0000	0.0000	0.0000	0.0000	0.0000	0.0000	0.0000	0.0000	0.0000	0.0000
Mg	0.0000	0.0000	0.0018	0.0000	0.0000	0.0000	0.0000	0.0008	0.0000	0.0000	0.0000	0.0000
Ca	1.7802	1.8115	1.6921	1.6077	1.5633	1.6061	1.6123	1.5836	1.7171	1.7501	1.8527	1.8341
Na	2.3752	2.3237	2.4652	2.5391	2.5890	2.4766	2.5177	2.5836	2.4483	2.3927	2.3259	2.2673
Total	20.11	20.12	20.13	20.13	20.13	20.08	20.11	20.14	20.13	20.11	20.16	20.08
An	0.43	0.43	0.40	0.38	0.37	0.39	0.39	0.38	0.41	0.42	0.44	0.44
Or	0.57	0.56	0.59	0.61	0.62	0.60	0.61	0.62	0.58	0.57	0.55	0.55
Ab	0.01	0.01	0.01	0.01	0.01	0.01	0.01	0.00	0.01	0.01	0.01	0.01

Table 2 Whole-rock geochemical data of Dongga gabbro, S. Tibet, China

Sample	DG12-05	DG12-06	DG12-08	DG12-18	DG12-19	DG12-20
Major elements (wt%)						
SiO ₂	49.30	48.45	52.27	48.84	49.06	48.33
TiO ₂	1.35	1.54	0.92	2.19	2.11	2.05
Al ₂ O ₃	16.11	16.30	17.48	15.50	15.79	15.38
TFe ₂ O ₃	10.85	11.77	10.43	11.03	10.60	11.21
MnO	0.18	0.18	0.26	0.10	0.10	0.10
MgO	6.50	6.33	4.08	6.86	6.61	7.00
CaO	10.12	9.36	8.15	10.75	10.84	11.11
Na ₂ O	3.26	3.38	3.51	2.62	2.65	2.58
K ₂ O	1.04	1.28	1.53	0.50	0.49	0.48
P ₂ O ₅	0.13	0.25	0.16	0.27	0.25	0.22
LOI	1.10	1.00	1.07	1.10	1.00	1.07
Mg [#]	51.88	49.19	41.32	52.82	52.88	52.92
Total	99.95	99.83	99.87	99.83	99.63	99.83
Trace elements (ppm)						
Li	8.4	12.2	9.7	13.4	9.6	9.9
Be	4.3	0.8	1.0	0.6	0.6	0.6
Sc	35.6	27.7	30.8	24.0	24.6	25.2
V	252.3	254.9	244.8	191.5	189.9	165.3
Cr	85.4	72.2	66.1	121.0	159.9	117.9
Co	30.8	54.8	30.3	47.4	51.3	48.4
Ni	54.1	56.6	47.5	184.4	180.4	188.7
Cu	57.4	130.0	136.5	63.7	66.8	40.4
Zn	76.6	98.1	72.0	60.0	61.3	59.2
Ga	18.5	19.6	18.0	17.1	17.4	17.2
Rb	18.0	22.8	23.7	14.1	12.0	11.5
Sr	360.8	407.2	335.0	414.6	456.1	435.4
Y	19.4	19.4	18.1	32.2	28.3	33.2
Zr	20.9	11.7	21.2	86.3	26.7	18.4
Nb	2.7	1.5	2.8	2.4	1.3	3.3
Sn	18.6	21.0	18.5	12.9	16.1	13.1
Cs	1.5	0.7	0.9	8.1	5.7	5.7
Ba	177.6	234.3	309.1	99.1	94.3	89.7
La	11.0	7.9	7.1	10.8	13.3	12.2
Ce	25.8	20.0	17.9	30.3	33.0	30.6
Pr	3.4	2.8	2.5	4.5	4.5	4.3
Nd	13.9	13.1	11.4	20.0	17.5	17.5
Sm	4.2	3.9	3.6	5.5	5.0	4.8
Eu	1.4	1.3	1.3	1.6	1.7	1.6
Gd	4.1	4.1	3.8	5.4	5.0	5.2
Tb	0.7	0.7	0.6	0.9	0.8	0.9
Dy	3.9	3.8	3.5	5.6	5.0	5.8
Ho	0.8	0.8	0.7	1.2	1.1	1.3
Er	2.1	2.1	1.9	3.6	3.1	3.7
Tm	0.3	0.3	0.3	0.6	0.5	0.6
Yb	1.9	1.7	1.5	3.9	3.0	4.1
Lu	0.3	0.2	0.2	0.6	0.5	0.6
Hf	1.4	0.9	1.5	2.4	1.1	0.9
Ta	0.4	0.3	0.4	0.5	0.5	0.4
Pb	5.4	4.9	6.2	1.3	1.8	1.3
Th	0.9	0.6	3.6	0.6	0.5	0.4
U	0.3	0.3	1.4	0.2	0.1	0.1

Mg[#]=Mg/(Mg+Fe²⁺) (molar ratio). LOI, loss on ignition

2008) was used to analyze results. The measured ²⁰⁴Pb was not applied for the common lead correction because the ²⁰⁶Pb/²⁰⁴Pb values of most analysis spots were larger than 1000. Concordia ages and diagrams were calculated using Isoplot at 95% confidence levels (Ludwig, 2003). The analytical data are summarized in Table 3.

3.4 Radiogenic isotopic systematics

3.4.1 Whole-rock Sr-Nd isotopes

About 100–150 mg whole-rock powder was completely decomposed in a HF-HClO₄ mixture for Sr-Nd isotopic

analysis. Sr and rare earth elements (REEs) were separated on quartz columns with a 5-ml AG 50W-X12 (200–400 mesh) resin bed. Nd was separated from other REEs on quartz columns using 1.7 ml Teflon[®] powder as a cation-exchange medium. Procedural blanks were <200 pg for Sr and <50 pg for Nd. For the measurements of isotopic composition, Sr was loaded with a Ta-HF activator on a single W filament and Nd was loaded as phosphate, and measurements were performed in a Re-double-filament configuration. The ¹⁴³Nd/¹⁴⁴Nd ratios were normalized to ¹⁴⁶Nd/¹⁴⁴Nd = 0.7219 and the ⁸⁷Sr/⁸⁶Sr ratios to ⁸⁶Sr/⁸⁸Sr = 0.1194. The isotopic ratios were measured using a Finnigan MAT-262 thermal ionization mass spectrometer in Laboratory for Radiogenic Isotope Geochemistry, University of Science and Technology of China, Hefei. Repeated measurements of La Jolla and NBS987 Sr standard solutions gave a mean value of 0.511869±0.000006 (2σ, n = 25) for the ¹⁴³Nd/¹⁴⁴Nd ratio and 0.710249±0.000012 (2σ, n = 38) for the ⁸⁷Sr/⁸⁶Sr ratio. Results of repeated Rb-Sr and Sm-Nd analyses on the standard material BCR-1 (basalt powder) gave a mean value of 0.705027±0.000013 for the ⁸⁷Sr/⁸⁶Sr ratio (n = 36; Rb, 46.54 ppm; Sr, 329.5 ppm) and 0.512633±0.000007 for the ¹⁴³Nd/¹⁴⁴Nd ratio (n = 45, Sm, 6.676 ppm; Nd, 28.77 ppm). The external precision is a 2 uncertainty based on replicate measurements on these standard solutions over one year. The raw data obtained were processed using the Isoplot program (Ludwig, 2003), giving 2 m error. The technical details of chemical separation and measurement are described in Chen et al. (2000, 2002, 2007).

3.4.2 In situ zircon Lu-Hf isotopes

In situ zircon Lu-Hf isotopes were measured by a New Wave UP 213 laser-ablation microprobe with a Neptune Multi-collector ICP-MS system at the Chinese Academy of Geological Science (CAGS), Beijing. Following the analytical procedures, including instrumental conditions and data acquisition, described by Hou et al. (2009), helium was used as a carrier gas to transport the ablated materials. The spot size was 55 μm and the repetition rate was 8 Hz. The analytical data were corrected using GJ1 as an external standard, which was measured twice every 5–10 analyses.

3.4.3 In situ plagioclase Rb-Sr isotopes

Plagioclase samples were prepared as thin sections thicker than 0.1 mm. In situ plagioclase Rb-Sr isotopic analysis was performed using a Nu Plasma multicollector sector ICP-MS, coupled to a 193 nm ArF excimer laser system at CCFS/GEMOC (Macquarie University). The Nu Plasma system uses a fixed detector array of 12 Faraday cups and three ion counters. In the system, beams are

Table 3 Zircon U-Pb isotopic data of Dongga gabbro, S. Tibet, China

Sample	Measured ratios							Ages (Ma)		
	$^{207}\text{Pb}/^{206}\text{Pb}$	$^{207}\text{Pb}/^{235}\text{U}$	$^{207}\text{Pb}/^{238}\text{U}$	$^{208}\text{Pb}/^{232}\text{Th}$	$^{208}\text{Pb}/^{235}\text{U}$	$^{207}\text{Pb}/^{206}\text{Pb}$	σ	$^{206}\text{Pb}/^{238}\text{U}$	σ	$^{206}\text{Pb}/^{238}\text{U}$
DG12-05-01	0.05802	0.00764	0.22073	0.02784	0.00165	0.00638	0.52	531.5	290.7	23.2
DG12-05-02	0.05795	0.00631	0.24560	0.02829	0.03093	0.00136	0.69	527.8	223.0	23.1
DG12-05-04	0.05892	0.00833	0.22831	0.03042	0.02894	0.00134	0.61	564.9	317.6	208.8
DG12-05-05	0.06207	0.00855	0.24011	0.03054	0.03019	0.00222	0.61	575.9	298.1	218.5
DG12-05-06	0.06461	0.01295	0.25902	0.02371	0.02977	0.00160	0.61	761.1	405.5	233.9
DG12-05-07	0.05823	0.00523	0.22918	0.01576	0.03025	0.00196	0.64	538.9	198.1	209.5
DG12-05-09	0.05029	0.00658	0.20785	0.02655	0.03024	0.00112	0.69	0.00073	0.52	209.3
DG12-05-10	0.10261	0.01922	0.26065	0.01815	0.02956	0.00233	0.57	1672.2	351.7	312.7
DG12-05-12	0.05086	0.00443	0.21316	0.02177	0.02924	0.00134	0.80	235.3	206.5	196.2
DG12-05-14	0.06147	0.01247	0.23331	0.04020	0.02921	0.00225	0.56	657.4	446.7	212.9
DG12-05-15	0.15311	0.02822	0.26125	0.05538	0.03097	0.00198	0.52	2381.2	318.7	515.4
DG12-05-18	0.05120	0.00509	0.20053	0.01770	0.02917	0.00071	0.84	250.1	32.4	185.6
DG12-05-19	0.10288	0.01429	0.26080	0.05155	0.03130	0.00149	0.61	1676.9	259.3	384.8
DG12-05-20	0.13398	0.04178	0.23976	0.07889	0.03199	0.00125	0.59	2150.9	570.5	370.1
DG12-05-21	0.06655	0.01172	0.29088	0.05018	0.03049	0.00154	0.56	833.3	374.1	259.3
DG12-05-23	0.08279	0.01190	0.28978	0.03210	0.02866	0.00172	0.54	1264.8	284.1	258.4
DG12-05-24	0.08709	0.01830	0.32183	0.04508	0.02969	0.00189	0.44	1362.7	413.4	283.3
DG12-05-25	0.07843	0.00948	0.33959	0.04502	0.03004	0.00149	0.58	1166.7	241.2	296.9
DG12-05-26	0.06169	0.00951	0.22153	0.02564	0.02906	0.00155	0.55	664.8	335.2	203.2
DG12-05-28	0.05107	0.00907	0.21398	0.03667	0.03096	0.00106	0.53	242.7	366.6	196.9
DG12-20-01	0.07664	0.01400	0.28452	0.03781	0.02905	0.00153	0.64	1122.2	372.4	254.2
DG12-20-02	0.05178	0.00592	0.20119	0.02264	0.02811	0.00102	0.61	276.0	244.4	186.1
DG12-20-03	0.05769	0.00820	0.23011	0.02573	0.03043	0.00135	0.71	516.7	210.3	21.3
DG12-20-04	0.05705	0.01032	0.20990	0.03285	0.02811	0.00109	0.69	494.5	407.4	193.5
DG12-20-05	0.07490	0.01298	0.20440	0.04796	0.02797	0.00171	0.86	1065.7	358.3	262.0
DG12-20-06	0.04937	0.00463	0.19447	0.01747	0.02878	0.00067	0.91	164.9	207.4	180.4
DG12-20-07	0.06080	0.00777	0.20103	0.03037	0.02868	0.00107	0.78	631.5	277.7	219.3
DG12-20-08	0.05323	0.00634	0.20149	0.02265	0.02831	0.00111	0.93	338.9	272.2	186.4
DG12-20-09	0.05732	0.00845	0.23563	0.02950	0.03075	0.00124	0.76	501.9	327.7	214.8
DG12-20-10	0.05889	0.00855	0.23355	0.03763	0.02923	0.00155	0.78	564.9	321.1	213.1
DG12-20-11	0.05009	0.00696	0.20266	0.02902	0.02944	0.00110	0.95	198.2	296.3	187.4
DG12-20-12	0.08745	0.01188	0.23151	0.04440	0.02974	0.00165	0.81	1372.2	264.8	290.7
DG12-20-13	0.05395	0.00361	0.22735	0.01636	0.03148	0.00161	0.68	368.6	208.0	13.5
DG12-20-14	0.05050	0.00662	0.24080	0.02376	0.03112	0.00183	0.53	587.1	242.6	219.1
DG12-20-15	0.09112	0.01059	0.21704	0.05807	0.02871	0.00225	0.51	1450.0	223.6	317.5
DG12-20-16	0.05930	0.00721	0.25734	0.03412	0.03136	0.00151	0.55	588.9	232.5	276.6

directed into the collectors by varying the dispersion of the instrument using an electrostatic zoom lens. The analyses were carried out using Nu Plasma time-resolved analysis software. The signal for each mass and ratio was monitored as a function of time during the analysis. This allowed us to select the more stable portions of the ablation for analysis before the data were processed to yield final results. It also allowed the analyst to recognize and exclude portions of the signal affected by inclusions or cracks and to terminate the analysis if the laser drilled through into an altered zone or into the matrix. Sr isotopes were analyzed on the same grains using an 85-mm spot size, 85% power (2.5 J/cm^2 fluence), and 200 s run time (60 s of background data collection followed by 140 s of sample data collection). The interference of ^{87}Rb on ^{87}Sr was corrected by measuring the intensity of ^{85}Rb and using $^{85}\text{Rb}/^{87}\text{Rb} = 0.38632$. This value was obtained by sequentially doping the Sr standard (QCD Analysts) with

Rb (Plasmachem Lot No: S4JS3700) and repeatedly measuring it to refine the value of $^{85}\text{Rb}/^{87}\text{Rb}$ necessary to give the true $^{87}\text{Sr}/^{86}\text{Sr}$ (Nowell and Parrish, 2001). The maximum $^{87}\text{Rb}/^{86}\text{Sr}$ value of the spiked solutions used in the refinement of the $^{85}\text{Rb}/^{87}\text{Rb}$ ratio was 0.3977.

4 Results

4.1 Whole-rock major- and trace-element geochemistry

Results of major- and trace-element analyses of representative samples are listed in Table 2 and plotted in Fig. 3a–c. All analyzed samples have low loss on ignition values (0.95wt%–1.36wt%), suggesting a low degree of alteration. The hornblende gabbro samples exhibit calc-alkaline suite, narrow compositional ranges of SiO_2 (48.33wt%–52.27wt%) and K_2O (0.48wt%–1.53wt%), and high contents of MgO (4.1wt%–7.0wt%) and TiO_2 (0.9wt%–2.2wt%). CaO content ranges between 8.15wt%

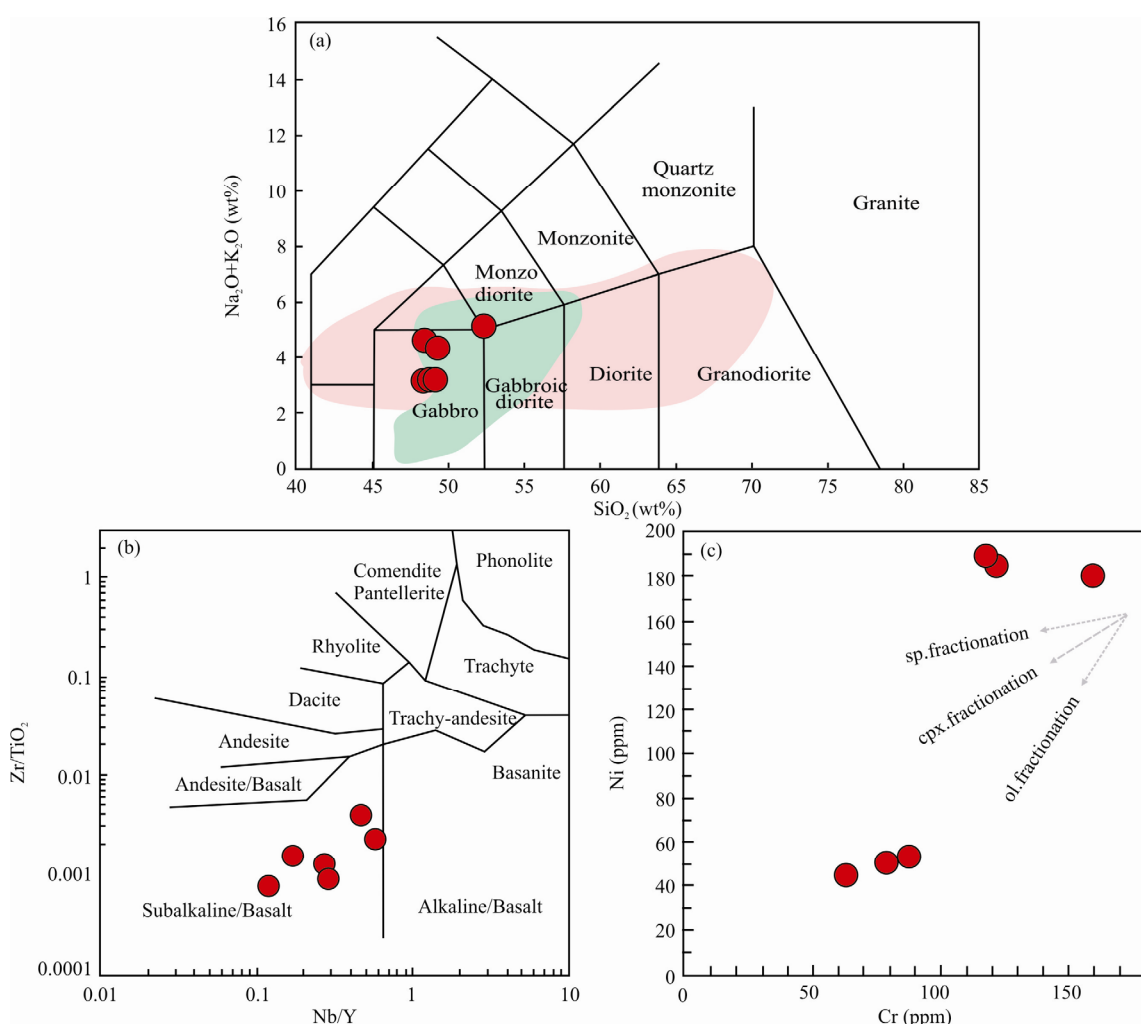


Fig. 3. (a) Plots of $(\text{K}_2\text{O}+\text{Na}_2\text{O})$ vs. SiO_2 (after Cox et al., 1979) for the Dongga gabbros, Sangri, and Yeba volcanic formations in southern Tibet. (b), Zr/TiO_2 vs. Nb/Y diagram (Winchester and Floyd, 1976) for the classification of the Dongga gabbros. (c), Ni vs. Cr diagram for the mineral fractionation of the Dongga gabbros. Sangri volcanic formations are from Kang et al. (2014); Yeba volcanic rocks are from Zhu et al. (2008).

and 11.11wt% and FeO content ranges between 15.38wt% and 15.79wt%. The samples show high concentrations of compatible elements (Cr: 66.1–159.93 ppm; Ni: 47.5–188.7 ppm, Fig. 3c). Chondrite-normalized REE patterns and primitive mantle-normalized trace element spidergrams are presented in Fig. 4. All analyzed samples have high total REE contents and show REE fractionation with relative enrichment of light REEs. The hornblende gabbros show less fractionation in the REEs ($\text{La}_N/\text{Yb}_N = 1.98\text{--}4.12$). The patterns of primitive mantle-normalized trace element spidergrams and chondrite-normalized REEs are similar to those of the Sangri Group volcanics (Fig. 4).

4.2 Zircon U-Pb geochronology and Lu-Hf isotopic systematics

Zircons from hornblende gabbro are euhedral, colorless, and transparent, ranging in size from 50 to 100 μm . The cathodoluminescence images show that the majority of the zircons exhibit concentric, oscillatory growth zoning, with high Th/U ratios from 0.43 to 1.14, indicative of their

genesis of igneous affinity (Griffin et al., 2002; Hoskin and Schaltegger, 2003). The results of zircon U-Pb dating are listed in Table 3, and plotted on U-Pb Concordia and weighted-average diagrams (Fig. 5). Sample DG12-20 yielded a weighted mean $^{206}\text{Pb}/^{238}\text{U}$ age of 185.5 ± 3.8 Ma (MSWD = 0.78) from 16 analyses of zircon grains. For sample DG12-05, 20 analyses of zircon grains yielded a weighted mean $^{206}\text{Pb}/^{238}\text{U}$ age of 189.5 ± 3.5 Ma (MSWD = 0.37). Results of Lu-Hf isotopic analyses of same grains in two samples in the Jurassic intrusions are listed in Table 5 and plotted in Fig. 6. Fifteen spot analyses of the same zircon grains from sample DG12-05 yielded variable eHf(t) values between +12.2 and +15.6 with initial $^{176}\text{Hf}/^{177}\text{Hf}$ ratios ranging from 0.283002 to 0.283095. Sample DG12-20 yielded eHf(t) values between +12.5 and +16.8 and initial $^{176}\text{Hf}/^{177}\text{Hf}$ ratios from 0.283006 to 0.283131.

4.3 Whole-rock Sr-Nd isotopic and in situ Sr isotopic systematics

Whole-rock Sr-Nd isotopic composition data for the

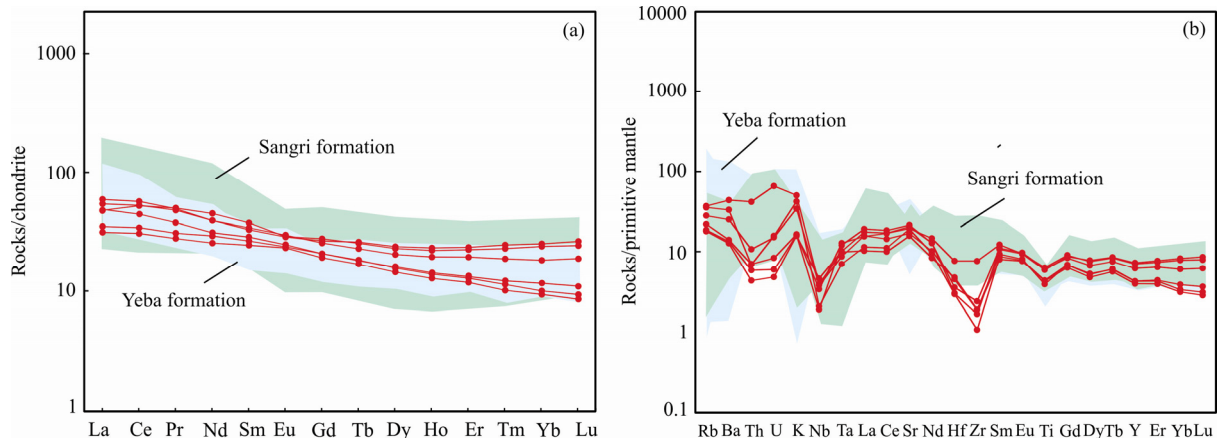


Fig. 4. Chondrite-normalized REE patterns (a) and primitive-mantle-normalized multi-element pattern (b) of the Dongga gabbros.

Chondrite and primitive mantle normalization values are from Sun and McDonough (1989).

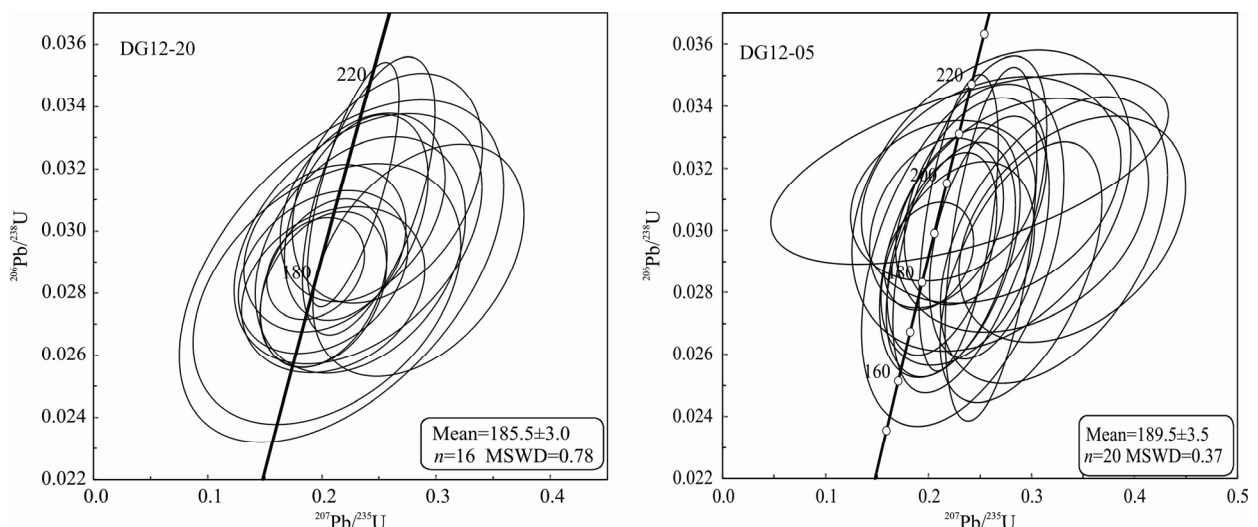


Fig. 5. Zircon U-Pb concordia diagrams of samples DG12-20 and DG12-05.

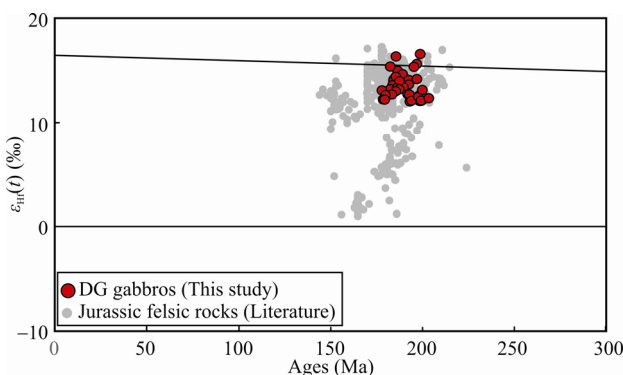


Fig. 6. $\varepsilon_{\text{Hf}}(t)$ vs age diagram of the Dongga gabbros and Jurassic granitoid rocks in southern Tibet.

Dongga gabbros are listed in Table 4. All Dongga hornblende gabbro samples show high values of $\varepsilon_{\text{Nd}}(t)$ (+4.90 to +6.99) and initial $^{87}\text{Sr}/^{86}\text{Sr}$ ratio (0.7033–0.7043). The Sr-Nd isotopic compositions of the hornblende gabbros are similar to those of Early Jurassic Sangri mafic rocks in southern Tibet (Zhu et al., 2008) but differ from those of the Yeba group (Zhu et al., 2008) (Fig. 7).

The results of in situ plagioclase Sr isotopic analyses are reported in Table 6 and shown in detail in Fig. 7b. From the core to the rim, the Sr isotopic compositions of six plagioclase crystals from different hornblende gabbros exhibit nearly consistent ratios. Moreover, these

Table 4 Whole-rock Sr and Nd isotopic data for the Dongga gabbro, S Tibet

Sample	$^{87}\text{Sr}/^{86}\text{Sr}$	2σ	$^{143}\text{Nd}/^{144}\text{Nd}$	2σ	$^{87}\text{Rb}/^{86}\text{Sr}$	$^{147}\text{Sm}/^{144}\text{Nd}$	$(^{87}\text{Sr}/^{86}\text{Sr})_i$	$\varepsilon_{\text{Nd}}(t)$	$t_{\text{DM}}^{\text{Nd}}$ (Ga)	$t_{\text{DM2}}^{\text{Nd}}$ (Ga)
DG12-05	0.703932	0.000010	0.512915	0.000008	0.124541	0.181956	0.703928	5.41	1.1	0.7
DG12-6-1	0.704196	0.000011	0.512889	0.000015	0.139544	0.180103	0.704192	4.90	1.2	0.7
DG12-6-2	0.704317	0.000015	0.512914	0.000012	0.176533	0.189740	0.704312	5.39	1.5	0.7
DG12-18	0.703334	0.000012	0.512974	0.000009	0.084682	0.165385	0.703331	6.56	0.6	0.5
DG12-19	0.703333	0.000014	0.512982	0.000010	0.065326	0.171840	0.703331	6.72	0.6	0.5
DG12-20	0.703354	0.000011	0.512996	0.000012	0.066029	0.165974	0.703352	6.99	0.5	0.5

$^{87}\text{Rb}/^{86}\text{Sr}$ and $^{147}\text{Sm}/^{144}\text{Nd}$ ratios are calculated using Rb, Sr, Sm and Nd contents by ICP-MS and measured $^{87}\text{Sr}/^{86}\text{Sr}$ and $^{143}\text{Nd}/^{144}\text{Nd}$ ratios by TIMS; $\varepsilon_{\text{Nd}}(t)$ values are calculated using present-day $(^{147}\text{Sm}/^{144}\text{Nd})_{\text{CHUR}} = 0.1967$ and $(^{143}\text{Nd}/^{144}\text{Nd})_{\text{CHUR}} = 0.512638$; t_{DM} values are calculated using present-day $(^{147}\text{Sm}/^{144}\text{Nd})_{\text{DM}} = 0.2135$ and $(^{143}\text{Nd}/^{144}\text{Nd})_{\text{DM}} = ^{87}\text{Rb}/^{86}\text{Sr}$ and $^{147}\text{Sm}/^{144}\text{Nd}$ ratios are calculated using Rb, Sr, Sm and Nd contents by ICP-MS and measured $^{87}\text{Sr}/^{86}\text{Sr}$ and $^{143}\text{Nd}/^{144}\text{Nd}$ ratios by TIMS; $\varepsilon_{\text{Nd}}(t)$ values are calculated using present-day $(^{147}\text{Sm}/^{144}\text{Nd})_{\text{CHUR}} = 0.1967$ and $(^{143}\text{Nd}/^{144}\text{Nd})_{\text{CHUR}} = 0.512638$; t_{DM2} values are calculated using present-day $(^{147}\text{Sm}/^{144}\text{Nd})_{\text{DM}} = 0.2135$ and $(^{143}\text{Nd}/^{144}\text{Nd})_{\text{DM}} = 0.51315$.

Table 5 Zircon Lu-Hf isotopic data of Dongga gabbro, S. Tibet, China

Sample	$^{176}\text{Hf}/^{177}\text{Hf}$	2σ	$^{176}\text{Yb}/^{177}\text{Hf}$	$^{176}\text{Lu}/^{177}\text{Hf}$	Age(Ma)	$\text{Hf}(0)$	$\text{Hf}(t)$	T_{DM}	T_{DM}^{C}
DG12-05-1	0.283093249	± 23	0.0842518	0.0023	186.0	11.4	15.2	232	257
DG12-05-2	0.283063639	± 31	0.0856433	0.0023	196.4	10.3	14.3	275	319
DG12-05-3	0.28305413	± 27	0.0631598	0.0016	183.9	10.0	13.8	284	342
DG12-05-4	0.283065881	± 32	0.0907300	0.0022	191.8	10.4	14.3	271	315
DG12-05-5	0.28305413	± 19	0.0631598	0.0016	189.1	10.0	13.9	284	339
DG12-05-6	0.283047955	± 19	0.0383697	0.0010	192.1	9.8	13.9	289	347
DG12-05-7	0.283025004	± 16	0.0561214	0.0016	192.0	8.9	13.0	326	403
DG12-05-8	0.283057299	± 21	0.0514264	0.0013	187.8	10.1	14.1	277	330
DG12-05-9	0.283076354	± 17	0.0601798	0.0012	185.8	10.8	14.7	250	287
DG12-05-10	0.283058549	± 19	0.0504681	0.0014	185.6	10.1	14.0	276	329
DG12-05-11	0.283102715	± 18	0.0504751	0.0012	196.6	11.7	15.9	212	221
DG12-05-12	0.28313085	± 23	0.0770429	0.0019	185.4	12.7	16.5	175	168
DG12-05-13	0.283128235	± 31	0.0548518	0.0014	198.7	12.6	16.8	176	163
DG12-05-14	0.283006462	± 23	0.0601015	0.0016	203.0	8.3	12.5	354	440
DG12-05-15	0.283017887	± 31	0.0882034	0.0021	193.6	8.7	12.7	341	423
DG12-05-16	0.28310655	± 78	0.0779514	0.0019	182.1	11.8	15.6	210	226
DG12-05-17	0.283082345	± 39	0.0645441	0.0018	188.6	11.0	14.9	245	277
DG12-05-18	0.283064822	± 20	0.0441828	0.0012	190.8	10.4	14.4	266	310
DG12-05-19	0.283067868	± 20	0.0636103	0.0017	184.7	10.5	14.3	265	311
DG12-05-20	0.283063464	± 20	0.0587598	0.0016	196.6	10.3	14.4	271	313
DG12-20-1	0.283034799	± 106	0.0637849	0.0018	184.6	9.3	13.1	314	314
DG12-20-2	0.283019162	± 18	0.0592951	0.0016	178.7	8.7	12.5	334	334
DG12-20-3	0.283003006	± 19	0.0504838	0.0014	193.2	8.2	12.2	357	357
DG12-20-4	0.283017887	± 31	0.0882034	0.0021	178.7	8.7	12.4	341	341
DG12-20-5	0.283034245	± 20	0.0593409	0.0016	177.8	9.3	13.0	313	390
DG12-20-6	0.283025929	± 27	0.0475286	0.0012	182.9	9.0	12.9	322	404
DG12-20-7	0.283042446	± 21	0.0585409	0.0016	182.3	9.6	13.4	301	369
DG12-20-8	0.283026929	± 22	0.0470375	0.0013	180.0	9.0	12.8	321	403
DG12-20-9	0.283094895	± 27	0.0478966	0.0011	195.2	11.4	15.6	223	223
DG12-20-10	0.283063464	± 27	0.0587598	0.0016	185.7	10.3	14.2	271	271
DG12-20-11	0.283042421	± 20	0.1114727	0.0026	187.1	9.6	13.4	310	310
DG12-20-12	0.283042207	± 27	0.0611589	0.0015	188.9	9.6	13.5	301	301
DG12-20-13	0.283033348	± 17	0.0905195	0.0022	199.8	9.2	13.3	320	320
DG12-20-14	0.283015352	± 18	0.0579646	0.0016	197.6	8.6	12.7	341	341
DG12-20-15	0.283042699	± 22	0.0369465	0.0009	182.5	9.6	13.5	295	295
DG12-20-16	0.28300228	± 19	0.0491801	0.0014	199.1	8.1	12.3	357	357

Age: zircon $^{206}\text{Pb}/^{238}\text{U}$ age. Decay constants: $\lambda\text{Lu}=1.865 \times 10^{-11} \text{ a}^{-1}$ (Scherer et al., 2001); $^{176}\text{Hf}/^{177}\text{Hf} = 0.282785$ (Bouvier et al., 2008); DM: $^{176}\text{Lu}/^{177}\text{Hf} = 0.0384$, $^{176}\text{Hf}/^{177}\text{Hf} = 0.283251$ (Griffin et al., 2000).

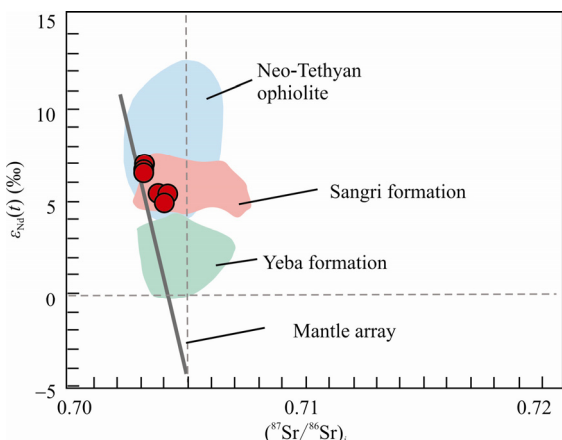


Fig. 7. $\varepsilon_{\text{Nd}}(t)$ vs. $(^{87}\text{Sr}/^{86}\text{Sr})_i$ diagram (after Chu et al., 2011) for the Dongga gabbros.

Data sources: IYTS ophiolites are from Mahoney et al. (1998) and Zhang et al. (2005); Sangri volcanic formations are from Kang et al. (2014); Yeba volcanic rocks are from Zhu et al. (2008).

compositions are similar to the whole-rock $^{87}\text{Sr}/^{86}\text{Sr}$ values of the host hornblende gabbro (Table 6).

5 Discussion

5.1 Effects of alteration, crustal contamination, and fractionation

5.1.1 Alteration and crustal assimilation

Crustal assimilation is inevitable for mantle-derived melts during their ascent through continental crust or their evolution within a crustal magma chamber (e.g., Castillo et al., 1999). However, the Sr-Nd-Hf isotopic

compositions of Dongga igneous zircons display mantle affinities (Fig. 8), indicating that only a minor crustal component was involved in the formation of these rocks. In general, the shallow-level assimilation of crustal materials causes an increase in $(^{87}\text{Sr}/^{86}\text{Sr})_i$ and a decrease in $\varepsilon_{\text{Nd}}(t)$ in magma suites (e.g., Rogers et al., 2000). The samples from the Dongga intrusions display radiogenic initial $(^{87}\text{Sr}/^{86}\text{Sr})_i$ ratios (0.7033–0.7043), low $^{144}\text{Nd}/^{143}\text{Nd}$ ratios (0.5129–0.5130), and positive $\varepsilon_{\text{Nd}}(t)$ (4.9–7.0, Fig. 8d), inconsistent with crustal assimilation. In addition, in situ $(^{87}\text{Sr}/^{86}\text{Sr})_i$ values in plagioclases from three different gabbro samples are similar to those of the host whole rock (Table 6), further discounting the possibility of intensive crustal assimilation during magma ascent. In addition, the juvenile signature of in situ zircon $\varepsilon_{\text{Hf}}(t)$ composition (+12.2 to +16.8, Table 5, Fig. 6) did not support crustal assimilation. The close consistency of in situ Sr isotopic compositions of different plagioclase crystals with the whole-rock $(^{87}\text{Sr}/^{86}\text{Sr})_i$ values of their host rocks further excludes crustal assimilation (Table 6). No systematic differences were observed between different crystals or host hornblende gabbros. This indicates that the plagioclases from the hornblende gabbros are isotopically well equilibrated. These $(^{87}\text{Sr}/^{86}\text{Sr})_i$ values from both plagioclases and their whole-rocks also do not show a trend pointing toward the composition [$(^{87}\text{Sr}/^{86}\text{Sr})_i = 0.7048$ –0.7062] of Jurassic granites from the Dongga area (Guo et al., 2013), which are considered as a potential crustal contaminant. Moreover, all samples of the Dongga mafic rocks have low Th contents ranging from 0.4 to 3.6

Table 6 In situ Rb-Sr isotopic data of plagioclase from Dongga gabbros, S. Tibet, China

Analysis No.	$^{87}\text{Sr}/^{86}\text{Sr}$ Meas	1σ	$^{86}\text{Sr}/^{88}\text{Sr}$ meas	1σ	$^{84}\text{Sr}/^{86}\text{Sr}$ Corr	1σ	^{85}Rb (V)	1σ
DG05-1	0.709827	0.00068	0.114241	0.000013	0.054768	0.000450	0.001534	0.000180
DG05-2	0.705816	0.00010	0.114190	0.000011	0.053848	0.000440	0.000509	0.000025
DG05-3	0.716307	0.00055	0.114236	0.000016	0.054480	0.000720	0.002789	0.000140
DG05-4	0.709140	0.00032	0.114247	0.000014	0.055641	0.000530	0.001316	0.000076
DG06-1	0.714902	0.00110	0.114272	0.000009	0.055758	0.000450	0.002612	0.000280
DG06-2	0.727743	0.00077	0.114278	0.000017	0.054584	0.000580	0.005815	0.000190
DG06-3	0.717373	0.00060	0.114314	0.000014	0.054206	0.000450	0.003319	0.000170
DG18-1	0.706247	0.00027	0.114357	0.000015	0.056964	0.000540	0.000526	0.000051
DG18-2	0.706253	0.00036	0.114296	0.000017	0.055958	0.000580	0.000531	0.000083
DG18-3	0.705636	0.00025	0.114310	0.000015	0.054703	0.000690	0.000484	0.000060
DG20-1	0.705636	0.00025	0.114310	0.000015	0.054703	0.000690	0.000484	0.000060
DG20-2	0.705960	0.00012	0.114320	0.000013	0.052729	0.000540	0.000553	0.000030
DG20-3	0.704751	0.00007	0.114347	0.000015	0.055274	0.000660	0.000249	0.000009
Analysis No.	$^{87}\text{Sr}/^{86}\text{Sr}$	1σ	Sr Int (V)	1σ	^{87}Rb	1σ		
DG05-1	0.703898	0.000090	0.1073290	0.008800	0.000619	0.000072		
DG05-2	0.703913	0.000069	1.100290	0.007200	0.000205	0.00001		
DG05-3	0.704228	0.000110	0.957789	0.004500	0.001125	0.000056		
DG05-4	0.703776	0.000077	1.031870	0.006500	0.000531	0.000031		
DG06-1	0.704077	0.000057	1.004120	0.005500	0.001053	0.00011		
DG06-2	0.704252	0.000098	1.014940	0.005000	0.002345	0.000077		
DG06-3	0.704139	0.000083	1.032440	0.010000	0.001338	0.000069		
DG18-1	0.703926	0.000087	0.956751	0.005100	0.000212	0.000021		
DG18-2	0.703915	0.000089	1.008010	0.007700	0.000214	0.000033		
DG18-3	0.703763	0.000083	1.097250	0.007500	0.000195	0.000024		
DG20-1	0.703763	0.000083	1.097250	0.007500	0.000195	0.000024		
DG20-2	0.703853	0.000090	1.093210	0.013000	0.000223	0.000012		
DG20-3	0.703734	0.000081	1.091830	0.013000	0.000101	0.0000038		

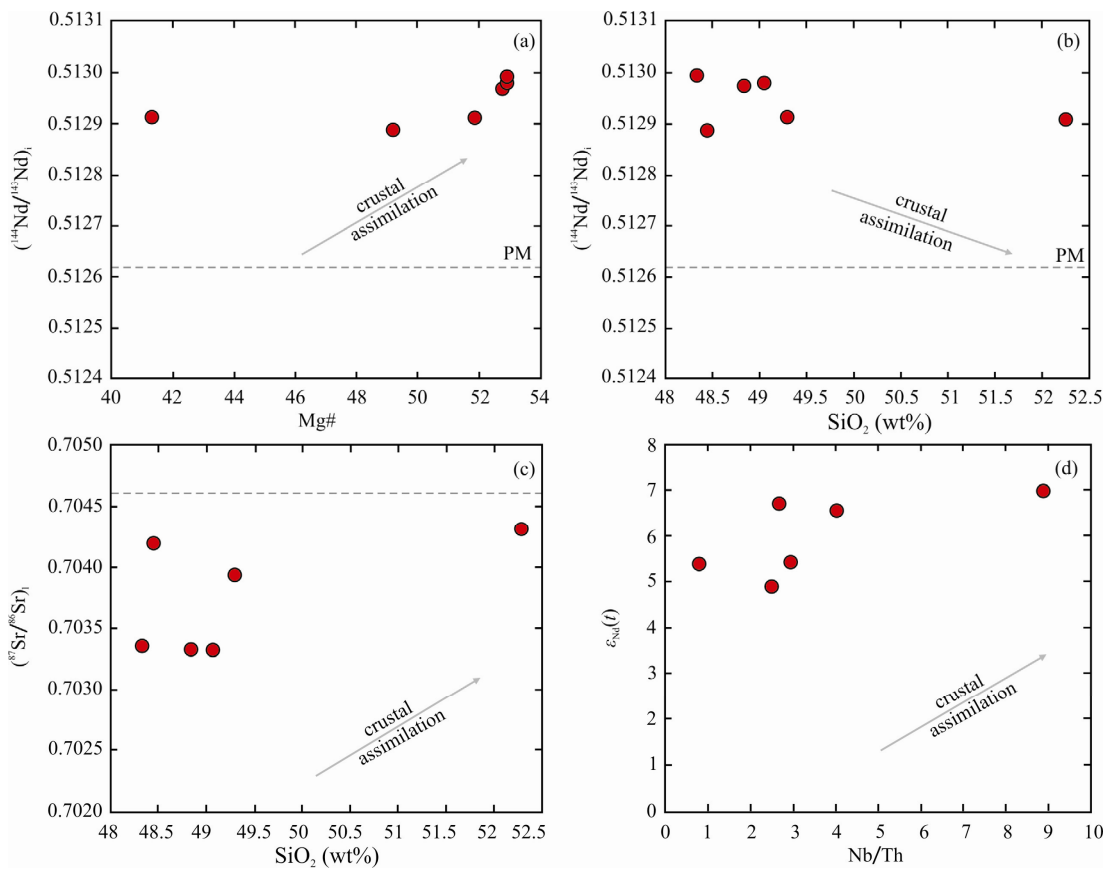


Fig. 8. Sr–Nd isotopic data vs. $Mg^{\#}$, SiO_2 , and trace element ratio diagrams for the Dongga gabbros. Primitive mantle ratios (dashed lines) are from Sun and McDonough (1989).

ppm (average 1.09 ppm), which are clearly lower than the average values for middle (6.5 ppm) and upper crust (10.5 ppm) (Rudnick and Gao, 2003), suggesting that crustal contamination did not play a significant role in their formation. Taking into account the negative correlation between $\varepsilon_{Nd}(t)$ and Nb/Th , $(^{87}Sr/^{86}Sr)_i$ and SiO_2 for mafic rock samples (Fig. 8d), we suggest that the Dongga mafic rocks did not undergo significant crustal contamination.

5.1.2 Fractional crystallization

Primary mantle-derived magma should contain an equilibrium partial melting of peridotites with $Ni > 400$ ppm, $Cr > 1000$ ppm, and $Mg^{\#} > 70$ (e.g. Frey et al., 1978). The Dongga mafic rocks have a MgO content between 4.1 and 7.0 wt% and a variable Ni content between 47.5 and 188.7 ppm, thus indicating a common fractional crystallization process among the intrusions. The negative correlations between Cr and Ni (Fig. 3c) suggest that the parental magmas for the Dongga mafic rocks probably experienced substantial clinopyroxene and/or combined olivine and spinel fractionation (Pfänder et al., 2002). With decreasing $Mg^{\#}$, Dongga gabbro shows a sharp decrease in Ni (Fig. 9e), but an almost constant total iron content (FeO^T) (Fig. 9d). This suggests that olivine

fractionation is the controlling factor affecting the whole-rock major- and trace-element compositions. This is consistent with the $Sc-Mg^{\#}$ and $Al_2O_3-Mg^{\#}$ correlations that Sc and Al_2O_3 deplete with decreasing $Mg^{\#}$ (Fig. 9a). The $Al_2O_3-Mg^{\#}$ ratio decreases with decreasing $Mg^{\#}$ (Fig. 9c), suggesting that clinopyroxene is also a major crystallizing phase. This is consistent with the Ni content decrease with decreasing $Mg^{\#}$. However, the lack of appropriate trends for Al_2O_3 and CaO/Al_2O_3 contents with decreasing $Mg^{\#}$ (Fig. 9c) and an insignificant Eu anomaly ($\delta Eu = 0.9\text{--}1.11$, Fig. 4) are not consistent with the plagioclase fractionation in the Dongga parental magmas.

5.2 Petrogenesis

5.2.1 Mantle source

The majority of volcanic arc magmas on earth are thought to have originated by the partial melting of the underlying mantle wedge (e.g., Handley et al., 2007; Pearce and Peate, 1995). In subduction zones, the magmatism is characterized by depletion of high field strength elements (HFSEs) due to retention of refractory minerals such as rutiles in the arc magma source and enrichment of large ion lithophile elements (LILEs) (such as Rb, Sr, Ba, Pb) and Th and U due to the addition of

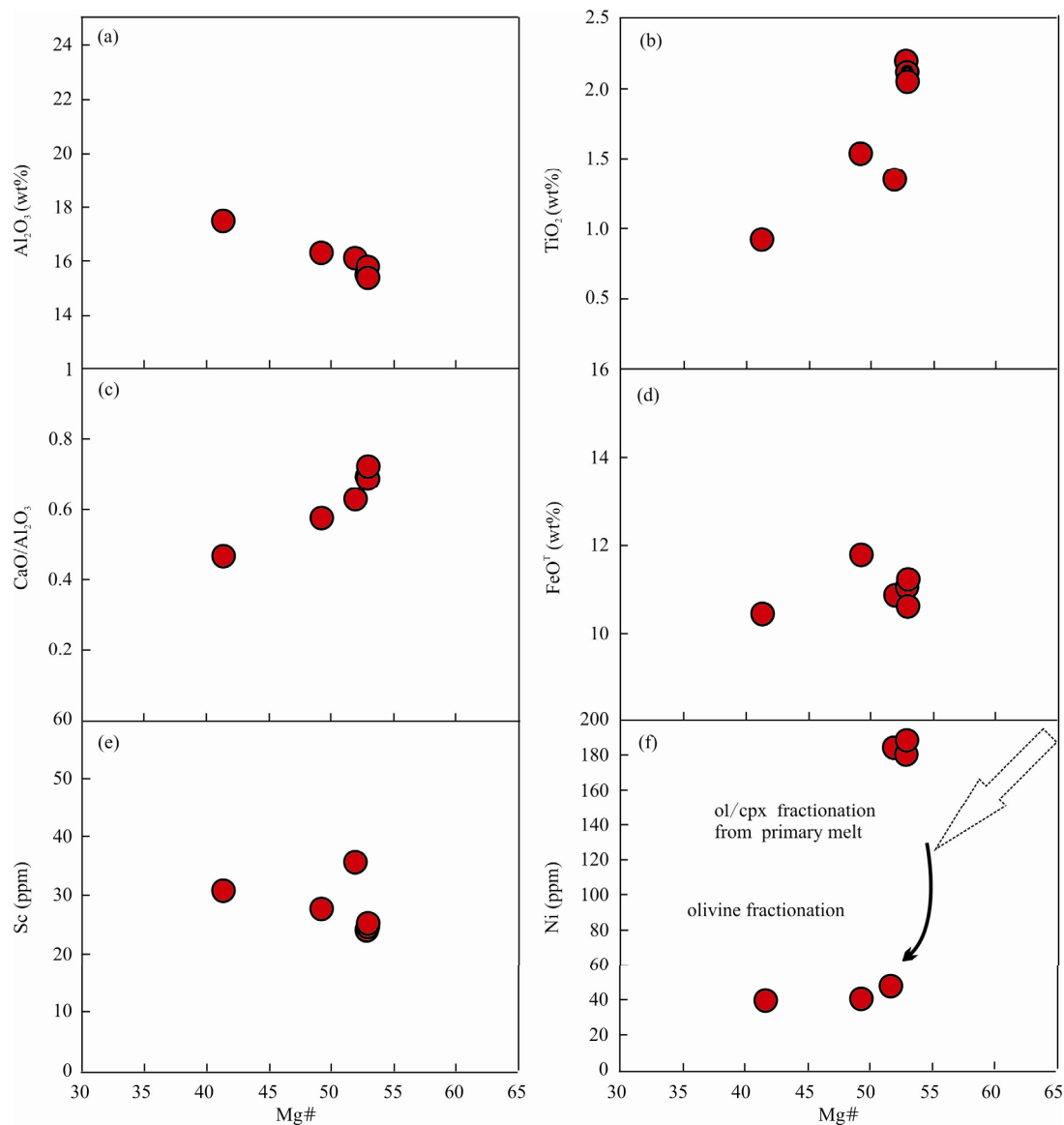


Fig. 9. Binary variation diagrams of the Dongga gabbros showing major- and trace-element variations as functions of Mg[#]. Mg[#] = 100 × Mg/(Mg + Fe²⁺). The crystallization trend is taken from Wang et al. (2012).

subducted input (e.g., Hawkesworth et al., 1997; Pearce and Peate, 1995). Likewise, the negative Nb-Ta and Ti anomalies of the volcanics along arc zones and active continental margins have been argued to result from retained rutiles during melting of subducted input (e.g., Ayers and Watson, 1993; Elliott et al., 1997; Stolz et al., 1996). Thus, the strong negative Nb-Ta and minor negative Ti anomalies of the Dongga gabbro are most likely due to rutile retention in the magma source (Fig. 4). Enrichment of Rb, Sr, Ba, Pb, Th, and U in the Dongga intrusion can be ascribed to the addition of subducted Tethyan-slab input.

Dongga gabbros have enriched Sr-Nd isotopic compositions compared with those of the Tethyan basalts of the Jurassic-Cretaceous ophiolites (Fig. 7) (Xu and

Castillo, 2004; Zhang et al., 2005), Indian MORBs (Chauvel and Blachert-Toft, 2001), which are interpreted to be derived from a subducted Neo-Tethyan oceanic slab (Zhu et al., 2009) (Fig. 9c). However, their Sr-Nd isotopic compositions and REE patterns are similar to those of Early Jurassic (190–174 Ma) mafic volcanic rocks of the Sangri Formation in southern Tibet (Fig. 7), which are considered to be derived from a mantle wedge (Kang et al., 2014). Moreover, not only the whole-rock samples, which may record the final isotopic compositions of magmas, but also zircons can record details of sequential contributions from isotopically distinct components in an evolving magma (e.g., Griffin et al., 2002), and zircon Hf isotopes are considered to be a powerful tool for tracing magma formation and evolution (e.g., Belousova et al., 2002). In

the case of the Dongga mafic rocks, the high $\varepsilon_{\text{Hf}}(t)$ values (+12.2 to +16.8) of the igneous zircons are generally consistent with examples from the mantle wedge-derived Triassic-Jurassic volcanic rocks and mantle magmas (Fig. 10). Moreover, Dongga gabbros fall in the fertile peridotite field, which is defined by the study of experimental melts (Falloon et al., 1988) and is characterized by high total Fe_2O_3 (>10wt%) and TiO_2 (>2wt%) (Table 2; Fig. 11). These features indicate that Dongga gabbros are derived from a relatively juvenile mantle enriched in major elements (e.g., lherzolite). This suggestion is consistent with high $\varepsilon_{\text{Nd}}(t)$ (4.9–7.0, Fig. 7), $\varepsilon_{\text{Hf}}(t)$ composition (12.2–16.8, Fig. 6), and low initial ($^{87}\text{Sr}/^{86}\text{Sr}$)_i ratios (0.7033–0.7043, Fig. 7). Therefore, the Dongga gabbros display mantle affinities and probably only a minor crustal component was involved in the formation of these rocks (Fig. 10). The depleted, MORB-like Nd–Hf isotopes suggest around 1% subducted-component input for the

mantle source of the Dongga gabbros. Such an amount (<1%) of the subducted-component input has a minor effect on the geochemical result; thus, the slab derived-fluid controls the budget of the LILEs (such as U, Th, and Pb; Fig. 4). The Dongga gabbros have a relatively large variation of Th/Nb (0.3–0.93) with a low and restricted U/Th (0.22–0.4) and Pb/Ce (0.1–0.2), pointing to the effect of the fluid-like component (Fig. 12; Elliott et al., 1997; Hawkesworth et al., 1997). We therefore propose that the Dongga gabbros were generated from a mantle wedge that was metasomatized by hydrous fluids.

5.2.2 Did the Dongga gabbros originate from a hydrous environment?

Volcanic arc magmas are thought to form by mantle wedge melting under hydrous influence (Grove et al., 2012). Many experimental studies have been devoted to find the evidence of crystallization of hydrous minerals and rocks, such as hornblende gabbros, from a hydrated tholeiitic magma typically derived from a metasomatized mantle wedge under an island arc (e.g., Takagi et al., 2005; Feig et al., 2006; Müntener and Ulmer, 2006). The results indicate that magmatic hornblendes can crystallize in gabbros from mafic magmas at the pressure, temperature, and water-enriched conditions expected in the magma chamber of island arcs (e.g., Zellmer et al., 2003). Petrological and geochemical evidences reveal that the Dongga gabbros accumulated from a water-enriched magma. First, the hornblende grains have a subhedral to anhedral texture, suggesting that they crystallized directly from a magma. Gabbros can generate from a dry mantle environment (e.g., dunite-troctolite-gabbro) or from a wet environment (e.g., dunite-wehrlite-hornblende gabbro) (Gaetani and Grove, 1998), thus crystallization of hornblende requires the magma to have a high water content (Sisson and Grove, 1993). Water-enriched basaltic magmas also often fractionate into, in order of appearance, olivine, clinopyroxene, and plagioclase (Sisson and Grove, 1993; Feig et al., 2006; Smith et al., 2009), and the most extreme end product of this process is the late crystallization of anorthite (Rollinson, 2010). This relationship is especially confirmed by the presence of anorthitic plagioclase in amphibole-bearing rocks in the Fiskenaesset complex, Greenland (Polat et al., 2009), and the Chimalpahad complex, India (Dharma Rao et al., 2011). In the Dongga gabbros, euhedral to subhedral plagioclase cuts across hornblende (Fig. 2e, g). Plagioclases rarely fill embayments in hornblende (Fig. 2b, h), which suggests that plagioclases crystallized after hornblende crystallization stopped. Some hornblende grains are enclosed within plagioclases (Fig. 2f), indicating crystallization of the hornblendes prior to plagioclase; this suggests the Dongga gabbros crystallized

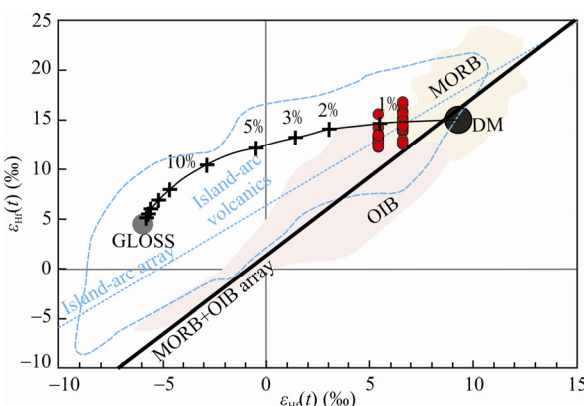


Fig. 10. Zircon $\varepsilon_{\text{Hf}}(t)$ vs. $\varepsilon_{\text{Nd}}(t)$ diagram for the Dongga gabbros.

Data sources: Field of Hf–Nd isotopic data for Indian MORB, OIB, and mantle array are from Chauvel and Blachert-Toft (2001) and Ingle et al. (2003). DM and GLOSS are from Chauvel et al. (2009), Plank and Langmuir (1998), Salters and Stracke (2004), and Workman and Hart (2005).

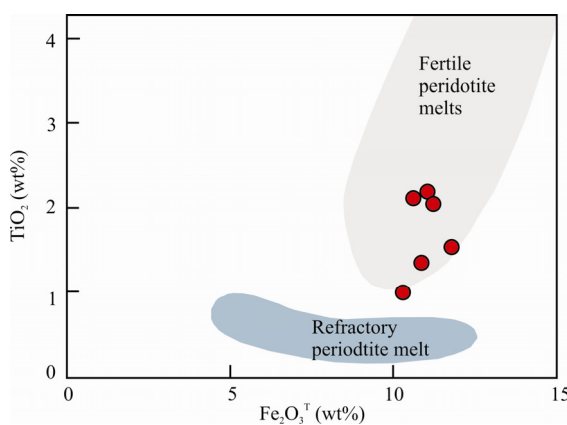


Fig. 11. $\text{Fe}_2\text{O}_3^{\text{T}}$ vs. TiO_2 diagram for the Dongga gabbros.

Fields for fertile and refractory peridotite melts are modified from Falloon et al. (1988).

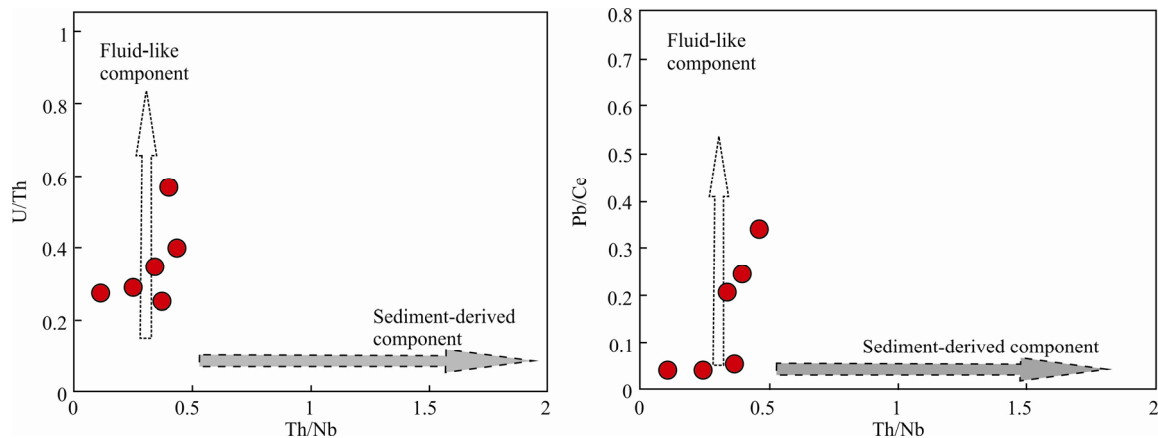


Fig. 12. Plots of U/Th and Pb/Ce vs. Th/Nb pointing to the effect of sediment-derived component (Singer et al., 2007).

from a water-enriched magma. Preferential crystallization of amphiboles over plagioclases is observed, indicating crystallization at high pressure and relatively high temperature (e.g., >250 MPa, >900 °C) and water-saturated conditions ($H_2O > 3\%$, Moore and Carmichael, 1998; Krawczynski et al., 2012). In addition to the amphiboles, experiments in a basaltic andesite system also demonstrated that the order of clinopyroxene crystallization is effected by magma water content. The order olivine-plagioclase-clinopyroxene in a dry system is changed to olivine-clinopyroxene-plagioclase in a water-saturated system (Gaetani et al. 1993). This was further quantified by Sisson and Grove (1993) and Feig et al. (2006) who demonstrated that plagioclase crystallizes before clinopyroxene at a low water content of <3wt% at pressures of >100 MPa, whereas plagioclase forms after clinopyroxene when the water content in the melt is >3wt%. In Dongga gabbro samples, certain hornblende grains contain clinopyroxene and display a gradational boundary reflecting earlier crystallization of clinopyroxene that reacted with water-rich magma to form hornblende (Fig. 2g). Thus, it is consistent with the postulation that plagioclases in the Dongga gabbros postdate the other phases, indicating the Dongga gabbros crystallized from a water-enriched magma.

In addition, the abundant presence of amphibole and dominance of anorthite (An values > 50) in the subduction-related arc gabbroic rocks has also been characterized by crystallization from hydrous source magmas (Prouteau et al., 2001; Costa et al., 2002). Anorthite has been widely observed in hydrous arc high-Al basalts and gabbroic nodules, forearc boninites, and gabbros (e.g., Crawford et al., 1987). Experimental studies have shown that the An component of plagioclase and K_D^{Ca-Na} (partition coefficient of Ca relative to Na between plagioclase and melt) between plagioclase and basalt increase with an increase in the H_2O content of melt (e.g., Sisson and Layne, 1993 and Takagi et al., 2005). The

presence of water raises the H_2O partial pressure, which in turn lowers the anorthite-albite liquidus and solidus temperatures and results in the crystallization of high An plagioclases (An > 50) (Sisson and Layne, 1993). This suggests that high H_2O content of the melt is preferable for the crystallization of An-rich plagioclase. Anorthites can crystallize from basalts with high H_2O content but not from a dry melt with normal arc magmas (Sisson and Grove 1993). The reason is explained by an experimental study showing that at pressures greater than 4 kbar, crystallization of liquidus Ca-rich clinopyroxene decreases the CaO/Na_2O ratio of the liquid, prohibiting the crystallization of high-An plagioclase from a hydrous tholeiite (Takagi et al. 2005). At moderate to high pressures (5–10 kbar, corresponding to middle-lower crustal levels), highly calcic plagioclase could crystallize from high-Al arc basalts with very high H_2O contents (~6%) (Panjasawatwong et al., 1995). This is consistent with the presence of amphibole and dominance of anorthite (An values > 50) in the Dongga gabbros, indicating they crystallized in a water-saturated parental melt.

The following petrological evidence suggests that the Dongga gabbros were crystallized in a water-rich source: 1) The existence of hornblende phenocrysts in the Dongga gabbros; 2) the late crystallization of plagioclase compared with other minerals; and 3) the domination of calcic plagioclase. Combined with their arc-type trace-element and Sr-Nd-Hf isotopic features, the petrological evidence suggests that the Dongga mafic intrusion was formed through hydrous melting of a mantle wedge metasomatized by aqueous fluids in response to the subduction of the Neo-Tethys slab.

5.2.3 Implications for Gangdese Jurassic crustal growth

Mafic magma underplating leading to crustal growth is commonly considered to have occurred during Neo-Tethyan Ocean subduction and India-Asia collision (Mo et

al., 2007; Chung et al., 2009). Widespread Cretaceous (ca. 80–95 Ma) felsic magmatism is considered to correspond directly with mafic magma underplating (e.g., Ma et al., 2015). The ~65–40 Ma Linzizong volcanic succession has been attributed to syn-collisional settings (Mo et al., 2005, 2007, 2008; Lee et al., 2009). These rocks suggested that 65–40 Ma basaltic underplating played a very important role in crustal growth and formation of the plateau (e.g., Mo et al., 2007; Chung et al., 2009). This study emphasizes the presence of Jurassic mantle-derived basaltic magmas in the southern Lhasa block, suggesting that underplating of basaltic magmas in Jurassic also played an important role in crustal growth of southern Tibet during Neo-Tethyan initiating subduction, similar to processes in Cretaceous and Eocene.

Recently, a number of Jurassic felsic magmatism (ca. 150–200 Ma) have been identified in the Gangdese batholith (e.g., Chu et al., 2011; Yang Zhiming et al., 2008; Guo et al., 2013; Hou et al., 2015). These Jurassic granitoids in southern Tibet are characterized by very high and positive $\varepsilon_{\text{Nd}}(t)$ (up to +7.5) and $\varepsilon_{\text{Hf}}(t)$ (up to +16.5) values indicating an important contribution from mantle-derived materials (Chung et al., 2005; Chu et al., 2011; Mo et al., 2005, 2007; Wen Daren, 2007; Ji et al., 2009; Zhu et al., 2011). These granitoids are thought to be generated through the processes of mantle-derived basaltic underplating and remelting. These granitoids are then involved in crustal melting and assimilation by primary basaltic magmas, magma storage at the base of the crust, and magma homogenization, as envisaged in the MASH model (Hildreth and Moorbath, 1988). Emplacement of the 180–190 Ma Dongga mafic intrusive rocks corresponds directly with the Early Jurassic magmatism in southern Tibet. Accordingly, their extreme high $\varepsilon_{\text{Nd}}(t)$ and $\varepsilon_{\text{Hf}}(t)$ values have implications for the petrogenesis of the Early Jurassic magmatic activity and the contribution of mantle-derived juvenile materials to crustal growth in the Dongga area and southern Tibet (Fig. 6e, g, Guo et al., 2013; Chung et al., 2009).

The hydrous partial melting of the lithosphere mantle triggered by dehydration in a subduction setting can create significant volumes of juvenile crust where appropriate basaltic sources are available in the middle-lower crust of intraoceanic arcs and active continental margins. The presence of anorthitic plagioclases and occurrence of hydrous mineral assemblages (amphibole + biotite) in the Dongga mafic rocks suggest an abundance of hydrous fluids during mafic magma generation as well as at later stages of magma evolution. The abundance of water likely triggered extensive melting of mantle peridotites to produce basaltic magmas (Tatsumi and Eggins, 1995) that were mainly underplated in the crust.

Geochemical features of magmas of the Dongga gabbros are interpreted to be generated by the northward subduction of Neo-Tethys beneath the southern Lhasa terrane as early as ~195 Ma. Coeval with a large volume of Late Triassic-Early Jurassic felsic intrusions within the Gangdese arc, the Gangdese Jurassic magmatic arc is interpreted to be initiated at a juvenile continental margin during the Late Triassic-Early Jurassic. However, the possibility of intraoceanic arc setting cannot be excluded by the present studies. The relationship established between crustal growth and lithospheric mantle melting in the Dongga region not only has important implications for the precollision development of the southern Lhasa sub-block but also may define the distribution of Jurassic porphyry deposits. From recent Jurassic mineralization studies, these Jurassic felsic magmatism can be further divided into two groups of distinct geochemical compositions (Hou et al., 2015). The ore-forming magma found in the southwestern part of this Jurassic arc has juvenile mantle-like isotopic compositions [$(^{87}\text{Sr}/^{86}\text{Sr})_i = 0.7041\text{--}0.7048$; $\varepsilon_{\text{Nd}}(t)$ as high as +7.5, and $\varepsilon_{\text{Hf}}(t)$ as high as +18]. In contrast, the Jurassic felsic magmatism found in the northeastern arc segment is isotopically less juvenile [$(^{87}\text{Sr}/^{86}\text{Sr})_i = 0.7041\text{--}0.7063$, $\varepsilon_{\text{Nd}}(t) < +4.5$, and $\varepsilon_{\text{Hf}}(t) < +12$; e.g., Yang Zhiming et al., 2008; Guo et al., 2013; Hou et al., 2015].

6 Conclusions

(1) The Dongga gabbros in southern Tibet were emplaced in the Late Cretaceous (ca. 185.5–189.5 Ma), suggesting occurrences of the Early Jurassic mafic magmatism along the Yarlung-Tsangpo suture zone.

(2) The Dongga gabbros are characterized by enrichment in large ion lithophile elements and light rare earth elements and depletion in high field strength elements relative to neighboring lithophile elements, which are signatures of arc magmatism, indicating that Dongga gabbros were generated by partial melting of the mantle.

(3) The petrological and mineral geochemical characteristics suggest that the Dongga gabbros were derived from a water-enriched source metasomatized by a fluid of Tethyan oceanic lithosphere. These results show that the hydrous partial melting of the lithosphere mantle triggered by dehydration in a subduction setting created the juvenile crust in southern Tibet.

(4) The Dongga gabbros indicate that the northward subduction of Neo-Tethyan oceanic lithosphere beneath the immature Lhasa continental margin developed prior to Early Jurassic.

Acknowledgments

The study was jointly supported by The National Key Research and Development Project of China (2016YFC0600310), National Science Foundation of China (41320104004; 41672197 and 41302054). We acknowledge the handling of editor Ziguang Hao and constructive comments from reviewers.

Manuscript received Dec. 6, 2016
accepted Jan. 27, 2017
edited by Fei Hongcai

References

- An, Z.S., Kutzbach, J.E., Prell, W.L., and Porter, S.C., 2001. Evolution of Asian monsoons and phased uplift of the Himalaya-Tibetan plateau since Late Miocene times. *Nature*, 411(6833): 62–66.
- Ayers, J.C., and Watson, E.B., 1993. Rutile solubility and mobility in supercritical aqueous fluids. *Contributions to Mineralogy and Petrology*, 114(3): 321–330.
- Belousova, E., Griffin, W., and O'Reilly, S.Y., 2002. Igneous zircon: trace element composition as an indicator of source rock type. *Contributions to Mineralogy and Petrology*, 143 (5): 602–622.
- Castillo, P.R., Janney, P.E., and Solidum, R.U., 1999. Petrology and geochemistry of Camiguin Island, southern Philippines: insights to the source of adakites and other lavas in a complex arc setting. *Contributions to Mineralogy and Petrology*, 134 (1): 33–51.
- Chauvel, C., and Blachert-Toft, J., 2001. A hafnium isotope and trace element perspective on melting of the depleted mantle. *Earth & Planetary Science Letters*, 190(3–4): 137–151.
- Chen, Y.H., Yang, J.S., Xiong, F.H., Zhang, L., Lai, S.M., and Chen, M., 2015. Geochronology and geochemistry of the subduction-related rocks with high Sr/Y ratios in the Zedong area: Implications for the magmatism in southern Lhasa terrane during Late Cretaceous. *Acta Geologica Sinica* (English Edition), 89: 351–368.
- Chu, M.F., Chung, S.L., Song, B., Liu, D.Y., O'Reilly, S.Y., Pearson, N.J., Ji, J.Q., and Wen, D.J., 2006. Zircon U-Pb and Hf isotope constraints on the Mesozoic tectonics and crustal evolution of southern Tibet. *Geology*, 34(9): 745–748.
- Chu, M.F., Chung, S.L., O'Reilly, S.Y., Pearson, N.J., Wu, F.Y., Li, X.H., Liu, D.Y., Ji, J.Q., Chu, C.H., and Lee, H.Y., 2011. India's hidden inputs to Tibetan orogeny revealed by Hf isotopes of Transhimalayan zircons and host rocks. *Earth and Planetary Science Letters*, 307(3–4): 479–486.
- Chung, S.L., Chu, M.F., Zhang, Y.Q., Xie, Y.W., Lo, C.H., Lee, T.Y., Lan, C.Y., Li, X.H., Zhang, Q., and Wang, Y.Z., 2005. Tibetan tectonic evolution inferred from spatial and temporal variations in post-collisional magmatism. *Earth-Science Reviews*, 68(3–4): 173–196.
- Chung, S.L., Chu, M.F., Ji, J.Q., O'Reilly, S.Y., Pearson, N.J., Liu, D.Y., Lee, T.Y., and Lo, C.H., 2009. The nature and timing of crustal thickening in Southern Tibet: Geochemical and zircon Hf isotopic constraints from postcollisional adakites. *Tectonophysics*, 477(1–2): 36–48.
- Cox, K.G., Bell, J.D., and Pankhurst, R.J., 1979. *The interpretation of igneous rocks*. London George Allen and Unwin: 595–602.
- Ding, L., Xu, Q., Yue, Y.H., Wang, H.Q., Cai, F.L., and Li, S., 2014. The Andean-type Gangdese Mountains: Paleoelevation record from the Paleocene-Eocene Linzhou Basin. *Earth & Planetary Science Letters*, 392: 250–264.
- Dong, Y.H., Xu, J.F., Zeng, Q.G., Wang, Q., Mao, G.Z., and Li, J., 2006. Is there a Neo-Tethys' subduction record earlier than arc volcanic rocks in the Sangri Group? *Acta Petrologica Sinica*, 22(3): 661–668 (in Chinese with English abstract).
- Elliott, T., Plank, T., Zindler, A., White, W., and Bourdon, B., 1997. Element transport from slab to volcanic front at the Mariana arc. *Journal of Geophysical Research Atmospheres*, 102(B7): 14991–15020.
- Falloon, T.J., Green, D.H., Hatton, C.J., and Harris, K.L., 1988. Anhydrous partial melting of a fertile and depleted peridotite from 2 to 30 kb and application to basalt petrogenesis. *Journal of Petrology*, 29(6): 1257–1288.
- Feig, S.T., Koepke, J., and Snow, J.E., 2006. Effect of water on tholeiitic basalt phase equilibria: an experimental study under oxidizing conditions. *Contributions to Mineralogy and Petrology*, 152(5): 611–638.
- Frey, F.A., Green, D.H., and Roy, S.D., 1978. Integrated models of basalt petrogenesis: A study of quartz tholeiites to olivine melilitites from south Eastern Australia utilizing geochemical and experimental petrological data. *Journal of Petrology*, 19 (3): 463–513.
- Gaetani, G.A., and Grove, T.L., 1998. The influence of water on melting of mantle peridotite. *Contributions to Mineralogy and Petrology*, 131(4): 323–346.
- Gaetani, G.A., Grove, T.L., and Bryan, W.B., 1993. The influence of water on the petrogenesis of subduction-related igneous rocks. *Nature*, 365(6444): 332–334.
- Geng, Q.R., Pan, G.T., Jin, Z.M., Wang, L.Q., Zhu, D.C., and Liao, Z.L., 2005. Geochemistry and genesis of the Yeba volcanic rocks in the Gangdese magmatic arc, Tibet. *Diqu Kexue-Zhongguo Dizhi Daxue Xuebao/Earth Science-Journal of China University of Geosciences*, 30(6): 747–760 (in Chinese with English abstract).
- Griffin, W.L., Powell, W.J., Pearson, N.J., and O'Reilly, S.Y., 2008. GLITTER: data reduction software for laser ablation ICP-MS. *Laser Ablation-ICP-MS in the earth sciences. Mineralogical association of Canada short course series*, 40: 204–207.
- Griffin, W.L., Wang, X., Jackson, S.E., Pearson, N.J., O'Reilly, S.Y., Xu, X., and Zhou, X., 2002. Zircon chemistry and magma mixing, SE China: In-situ analysis of Hf isotopes, Tonglu and Pingtan igneous complexes. *Lithos*, 61(3): 237–269.
- Grove, T.L., Till, C.B., and Krawczynski, M.J., 2012. The role of H_2O in subduction zone magmatism. *Annual Review of Earth and Planetary Sciences*, 40: 413–439.
- Guo, L.S., Liu, Y.L., Liu, S.W., Cawood, P.A., Wang, Z.H., and Liu, H.F., 2013. Petrogenesis of Early to Middle Jurassic granitoid rocks from the Gangdese belt, Southern Tibet: Implications for early history of the Neo-Tethys. *Lithos*, 179 (5): 320–333.
- Handley, H.K., 2007. Constraining fluid and sediment contributions to subduction-related magmatism in Indonesia: Ijen volcanic complex. *Journal of Petrology*, 48(6): 1155–1183.

- Hawkesworth, C.J., Turner, S.P., McDermott, F., Peate, D.W., and Van, C.P., 1997. U-Th isotopes in arc magmas: Implications for element transfer from the subducted crust. *Science*, 276(5312): 551–555.
- Hildreth, W., and Moorbath, S., 1988. Crustal contributions to arc magmatism in the Andes of Central Chile. *Contributions to Mineralogy and Petrology*, 98(4): 455–489.
- Hou, Z.Q., Gao, Y.F., Qu, X.M., Rui, Z.Y., and Mo, X.X., 2004. Origin of adakitic intrusives generated during mid-Miocene east–west extension in southern Tibet. *Earth and Planetary Science Letters*, 220(1–2): 139–155.
- Hou, Z.Q., Yang, Z.M., Qu, X.M., Meng, X.J., Li, Z.Q., Beaudoin, G., Rui, Z.Y., Gao, Y.F., and Zaw, K., 2009. The Miocene Gangdese porphyry copper belt generated during post-collisional extension in the Tibetan Orogen. *Ore Geology Reviews*, 36(1–3): 25–51.
- Hou, Z.Q., Zheng, Y.C., Yang, Z.M., Rui, Z.Y., Zhao, Z.D., Jiang, S.H., Qu, X.M., and Sun, Q.Z., 2013. Contribution of mantle components within juvenile lower-crust to collisional zone porphyry Cu systems in Tibet. *Mineralium Deposita*, 48(2): 173–192.
- Hou, Z.Q., Yang, Z.M., Lu, Y.J., Kemp, A., Zheng, Y.C., Li, Q.Y., Tang, J.X., Yang, Z.S., and Duan, L.F., 2015. A genetic linkage between subduction-and collision-related porphyry Cu deposits in continental collision zones. *Geology*, 43(3): 247–250.
- Hoskin, P.W.O., 2003. The composition of zircon and igneous and metamorphic petrogenesis. *Rev. Miner. Geochem.*, 53(1): 27–62.
- Ingle, S., Weis, D., Doucet, S., and Mattielli, N., 2003. Hf isotope constraints on mantle sources and shallow-level contaminants during Kerguelen hot spot activity since ~120 Ma. *Geochemistry Geophysics Geosystems*, 4(8): 8.
- Jackson, S.E., Pearson, N.J., Griffin, W.L., and Belousova, E.A., 2004. The application of laser ablation-inductively coupled plasma-mass spectrometry to in situ U–Pb zircon geochronology. *Chemical Geology*, 211(1–2): 47–69.
- Ji, W.Q., Wu, F.Y., Chung, S.L., Li, J.X., and Liu, C.Z., 2009. Zircon U–Pb geochronology and Hf isotopic constraints on petrogenesis of the Gangdese batholith, southern Tibet. *Chemical Geology*, 262(3–4): 229–245.
- Kang, Z.Q., Xu, J.F., and Chen, J.L., 2010. The geochronology of Sangri Group volcanic rocks in Tibet: Constraints from later Mamen intrusions. *Geochimica*, 39(6): 520–530 (in Chinese with English abstract).
- Kang, Z.Q., Xu, J.F., Chen, J.L., and Wang, B.D., 2009. Geochemistry and origin of Cretaceous adakites in Mamuxia Formation, Sangri Group, South Tibet. *Geochimica*, 38(4): 334–344 (in Chinese with English abstract).
- Kang, Z.Q., Xu, J.F., Wilde, S.A., Feng, Z.H., Chen, J.L., Wang, B.D., Fu, W.C., and Pan, H.B., 2014. Geochronology and geochemistry of the Sangri Group volcanic rocks, southern Lhasa terrane: Implications for the early subduction history of the Neo-Tethys and Gangdese magmatic arc. *Lithos*, 200–201(1): 157–168.
- Kapp, P., Yin, A., Harrison, T.M., and Ding, L., 2005. Cretaceous-Tertiary shortening, basin development, and volcanism in central Tibet. *Geological Society of America Bulletin*, 117(7–8): 865–878.
- Krawczynski, M.J., Grove, T.L., and Behrens, H., 2012. Amphibole stability in primitive arc magmas: effects of temperature, H_2O content, and oxygen fugacity. *Contributions to Mineralogy and Petrology*, 164(2): 317–339.
- Lee, H.Y., Chung, S.L., Lo, C.H., Ji, J.Q., Lee, T.Y., Qian, Q., and Zhang, Q., 2009. Eocene Neotethyan slab breakoff in southern Tibet inferred from the Linzizong volcanic record. *Tectonophysics*, 477(1–2): 20–35.
- Ludwig, K.R., 2000. Users manual for ISOPLOT/EX, version 2. A geochronological toolkit for Microsoft Excel.
- Lv, X., Wang, Z.H., Liu, Y.L., Liu, H.F., Xu, K.F., and Zhang, J.S., 2015. Geochronology and geochemistry of the Late Cretaceous to Paleocene intrusions in East Gangdese, Lhasa, Tibet and their tectonic significances. *Acta Geologica Sinica* (English Edition), 89(2): 441–466.
- Ma, L., Wang, Q., Wyman, D.A., Jiang, Z.Q., Wu, F.Y., Li, X.H., Yang, J.H., Gou, G.N., and Guo, H.F., 2015. Late Cretaceous back-arc extension and arc system evolution in the Gangdese area, southern Tibet: Geochronological, petrological, and Sr–Nd–Hf–O isotopic evidence from Dagze diabases. *Journal of Geophysical Research: Solid Earth*, 120(9): 6159–6181.
- Mo, X.X., Dong, G.C., Zhao, Z.D., Guo, T.Y., Wang, L.L., and Chen, T., 2005. Timing of magma mixing in the Gangdisê magmatic belt during the India-Asia collision: Zircon SHRIMP U–Pb dating. *Acta Geologica Sinica* (English Edition), 79(1): 66–76.
- Mo, X.X., Hou, Z.Q., Niu, Y.L., Dong, G.C., Qu, X.M., Zhao, Z.D., and Yang, Z.M., 2007. Mantle contributions to crustal thickening during continental collision: Evidence from Cenozoic igneous rocks in southern Tibet. *Lithos*, 96(1–2): 225–242.
- Mo, X.X., Niu, Y.L., Dong, G.C., Zhao, Z.D., Hou, Z.Q., Zhou, S., and Ke, S., 2008. Contribution of syncollisional felsic magmatism to continental crust growth: A case study of the Paleogene Linzizong volcanic Succession in southern Tibet. *Chemical Geology*, 250(1): 49–67.
- Molnar, P., England, P., and Martinod, J., 1993. Mantle dynamics, uplift of the Tibetan Plateau, and the Indian Monsoon. *Reviews of Geophysics*, 31(4): 357–396.
- Moore, G., and Carmichael, I.S.E., 1998. The hydrous phase equilibria (to 3 kbar) of an andesite and basaltic andesite from western Mexico: constraints on water content and conditions of phenocryst growth. *Contributions to Mineralogy and Petrology*, 130(3): 304–319.
- Müntener, O., Kelemen, P.B., and Grove, T.L., 2001. The role of H_2O during crystallization of primitive arc magmas under uppermost mantle conditions and genesis of igneous pyroxenites: an experimental study. *Contributions to Mineralogy and Petrology*, 141(6): 643–658.
- Panjasawatwong, Y., Danyushhevsky, L.V., Crawford, A.J., and Harris, K.L., 1995. An experimental study of the effects of melt composition on plagioclase–melt equilibria at 5 and 10 kbar: implications for the origin of magmatic high-An plagioclase. *Contributions to Mineralogy and Petrology*, 118(4): 420–432.
- Pearce, J.A., and Peate, D.W., 1995. Tectonic implications of the composition of volcanic ARC magmas. *Earth and Planetary Sciences*, 23(23): 251–285.
- Pfänder, J.A., Jochum, K., Kozakov, I., Kröner, A., and Todt, W., 2002. Coupled evolution of back-arc and island arc-like mafic crust in the late-Neoproterozoic Agardagh Tes-Chem ophiolite, Central Asia: evidence from trace element and Sr–

- Nd–Pb isotope data. *Contributions to Mineralogy and Petrology*, 143(2): 154–174.
- Plank, T., and Langmuir, C.H., 1998. The chemical composition of subducting sediment and its consequences for the crust and mantle. *Chemical Geology*, 145(3): 325–394.
- Polat, A., Appel, P.W.U., Fryer, B., Windley, B., Frei, R., Samson, I.M., and Huang, H., 2009. Trace element systematics of the Neoarchean Fiskenæsset anorthosite complex and associated meta-volcanic rocks, SW Greenland: Evidence for a magmatic arc origin. *Precambrian Research*, 175(1–4): 87–115.
- Prouteau, G., Scaillet, B., Pichavant, M., and Maury, R., 2001. Evidence for mantle metasomatism by hydrous silicic melts derived from subducted oceanic crust. *Nature*, 410(6825): 197–200.
- Pullen, A., Kapp, P., Gehrels, G.E., Decelles, P.G., Brown, E.H., Fabijanic, J.M., and Ding, L., 2008. Gangdese retroarc thrust belt and foreland basin deposits in the Damxung area, southern Tibet. *Journal of Asian Earth Sciences*, 33(5–6): 323–336.
- Qu, X.M., Hou, Z., Zaw, K., and Li, Y.G., 2007. Characteristics and genesis of Gangdese porphyry copper deposits in the southern Tibetan Plateau: Preliminary geochemical and geochronological results. *Ore Geology Reviews*, 31(1–4): 205–223.
- Rogers, N., Macdonald, R., Fitton, J.G., George, R., Smith, M., and Barreiro, B., 2000. Two mantle plumes beneath the East African rift system: Sr, Nd and Pb isotope evidence from Kenya Rift basalts. *Earth & Planetary Science Letters*, 176(3): 387–400.
- Rollinson, H., 2010. Coupled evolution of Archean continental crust and subcontinental lithospheric mantle. *Geology*, 38(12): 1083–1086.
- Rudnick, R.L., and Gao, S., 2003. *Composition of Continental Crust*. Treatise on geochemistry, 3: 659.
- Salters, V.J.M., and Stracke, A., 2004. Composition of the depleted mantle. *Geochemistry Geophysics Geosystems*, 5(5): 469–484.
- Sisson, T.W., and Layne, G.D., 1993. H₂O in basalt and basaltic andesite glass inclusions from four subduction-related volcanoes. *Earth & Planetary Science Letters*, 117(3–4): 619–635.
- Sisson, T.W., and Grove, T.L., 1993. Experimental investigations of the role of H₂O in calc-alkaline differentiation and subduction zone magmatism. *Contributions to Mineralogy and Petrology*, 113(2): 143–166.
- Smith, D.J., Petterson, M.G., Saunders, A.D., Millar, I.L., Jenkin, G.R.T., Toba, T., Naden, J., and Cook, J.M., 2009. The petrogenesis of sodic island arc magmas at Savo volcano, Solomon Islands. *Contributions to Mineralogy and Petrology*, 158(6): 785–801.
- Stoltz, A.J., Jochum, K.P., Spettel, B., and Hofmann, A.W., 1996. Fluid- and melt-related enrichment in the subarc mantle: Evidence from Nb/Ta variations in island-arc basalts. *Geology*, 24(7): 587–590.
- Sun, S.S., and McDonough, W.F., 1989. Chemical and isotopic systematics of oceanic basalts; Implications for mantle composition and processes. *Geological Society London Special Publications*, 42(1): 313–345.
- Takagi, D., Sato, H., and Nakagawa, M., 2005. Experimental study of a low-alkali tholeiite at 1–5 kbar: optimal condition for the crystallization of high-An plagioclase in hydrous arc tholeiite. *Contributions to Mineralogy and Petrology*, 149(5): 527–540.
- Tang, J.X., Li, F.J., Li, Z.J., Zhang, L., Tang, X.Q., Deng, Q., Lang, X.H., Huang, Y., Yao, X.F., and Wang, Y., 2010. Time limit for formation of main geological bodies in Xiongecun copper-gold deposit, Xietongmen County, Tibet: Evidence from zircon U-Pb ages and Re-Os age of molybdenite. *Mineral Deposits*, 29(3): 461–475 (in Chinese with English abstract).
- Tatsumi, Y., and Eggins, S., 1995. *Subduction zone magmatism*. Wiley.
- Wang, C., Ding, L., Zhang, L.Y., Kapp, P., Pullen, A., and Yue, Y.H., 2016. Petrogenesis of Middle–Late Triassic volcanic rocks from the Gangdese belt, southern Lhasa terrane: Implications for early subduction of Neo-Tethyan oceanic lithosphere. *Lithos*, 262: 320–333.
- Wang, R., Yang, Z.M., Dufrane, S.A., Richards, J.P., and Hou, Z.Q., 2014a. Increased magmatic water content—The key to Oligo-Miocene porphyry Cu–Mo ± Au formation in the eastern Gangdese belt, Tibet. *Economic Geology*, 109(109): 1315–1339.
- Wang, R., Richards, J.P., Hou, Z.Q., and Yang, Z.M., 2014b. Extent of underthrusting of the Indian plate beneath Tibet controlled the distribution of Miocene porphyry Cu–Mo ± Au deposits. *Mineralium Deposita*, 49(2): 165–173.
- Wang, R., Richards, J.P., Hou, Z.Q., Yang, Z.M., Gou, Z.B., and Dufrane, S.A., 2014c. Increasing magmatic oxidation state from paleocene to miocene in the eastern Gangdese Belt, Tibet: implication for collision-related porphyry Cu–Mo±Au mineralization. *Economic Geology*, 109(7): 1943–1965.
- Wang, R., Richards, J.P., Hou, Z.Q., An, F., and Creaser, R.A., 2015. Zircon U–Pb age and Sr–Nd–Hf–O isotope geochemistry of the Paleocene–Eocene igneous rocks in western Gangdese: Evidence for the timing of Neo-Tethyan slab breakoff. *Lithos*, 224: 179–194.
- Wang, X.C., Li, Z.X., Li, X.H., Li, J., Liu, Y., Long, W.G., Zhou, J.B., and Wang, F., 2011. Temperature, pressure, and composition of the mantle source region of Late Cenozoic basalts in Hainan Island, SE Asia: a consequence of a young thermal mantle plume close to subduction zones? *Journal of Petrology*: r61.
- Wen, D.R., 2007. The Gangdese batholith, Southern Tibet. Ages, geochemical characteristics and petrogenesis. Unpublished Ph.D. thesis, National Taiwan University, (120 pp.).
- Winchester, J.A., and Floyd, P.A., 1976. Geochemical magma type discrimination: application to altered and metamorphosed basic igneous rocks. *Earth & Planetary Science Letters*, 28(3): 459–469.
- Workman, R.K., and Hart, S.R., 2005. Major and trace element composition of the depleted MORB mantle (DMM). *Earth & Planetary Science Letters*, 231(1–2): 53–72.
- Wu, F.Y., Ji, W.Q., Liu, C.Z., and Chung, S.L., 2010. Detrital zircon U–Pb and Hf isotopic data from the Xigaze fore-arc basin: Constraints on Transhimalayan magmatic evolution in southern Tibet. *Chemical Geology*, 271(1–2): 13–25.
- Xiong, Q., Griffin, W.L., Zheng, J.P., O'Reilly, S.Y., Pearson, N.J., Xu, B., and Belousova, E.A., 2016. Southward trench migration at ~130–120 Ma caused accretion of the Neo-Tethyan forearc lithosphere in Tibetan ophiolites. *Earth & Planetary Science Letters*, 438: 57–65.

- Xu, B., Griffin, W.L., Xiong, Q., Hou, Z.Q., O'Reilly, S.Y., Guo, Z., Pearson, N.J., Gréau, Y., Yang, Z.M., and Zheng, Y.C., 2017. Ultrapotassic rocks and xenoliths from South Tibet: Contrasting styles of interaction between lithospheric mantle and asthenosphere during continental collision. *Geology*, 45 (1): 51–54.
- Xu, J.F., and Castillo, P.R., 2004. Geochemical and Nd-Pb isotopic characteristics of the Tethyan asthenosphere: implications for the origin of the Indian Ocean mantle domain. *Tectonophysics*, 393(1–4): 9–27.
- Yang, Z.M., 2008. The Qulong giant porphyry copper deposit in Tibet. Magmatism and mineralization. Unpublished Ph.D. thesis, Institute of Geology Chinese Academy of Geological Sciences, Beijing, (144 pp. (in Chinese with English abstract)).
- Yang, Z.M., Hou, Z.Q., White, N.C., Chang, Z.S., Li, Z.Q., and Song, Y.C., 2009. Geology of the post-collisional porphyry copper–molybdenum deposit at Qulong, Tibet. *Ore Geology Reviews*, 36(1–3): 133–159.
- Yang, Z.M., Lu, Y.J., Hou, Z.Q., and Chang, Z.S., 2015. High-Mg diorite from Qulong in southern Tibet: Implications for the genesis of adakite-like intrusions and associated porphyry Cu deposits in collisional orogens. *Journal of Petrology*, 56 (2): 227–254.
- Yin, A., and Harrison, T.M., 2003. Geologic Evolution of the Himalayan-Tibetan Orogen. *Annual Review of Earth & Planetary Sciences*, 28(28): 211–280.
- Zellmer, G.F., Hawkesworth, C.J., Sparks, R.S.J., Thomas, L.E., Harford, C.L., Brewer, T.S., and Loughlin, S.C., 2003. Geochemical evolution of the Soufrière Hills volcano, Montserrat, Lesser Antilles volcanic arc. *Journal of Petrology*, 29(8): 1349–1374.
- Zhang, H.F., Xu, W.C., Guo, J.Q., Zong, K.Q., Cai, H.M., Yuan, H.L., 2007. Zircon U-Pb and Hf isotopic composition of deformed granite in the southern margin of the Gangdese Belt, Tibet: evidence for early Jurassic subduction of Neo-Tethyan oceanic slab. *Acta Petrologica Sinica* 23(6), 1347–1353 (in Chinese with English abstract).
- Zhang, S.Q., Mahoney, J.J., Mo, X.X., Ghazi, A.M., Milani, L., Crawford, A.J., Guo, T.Y., and Zhao, Z.D., 2004. Evidence for a Widespread Tethyan Upper Mantle with Indian-Ocean-Type Isotopic Characteristics. *Journal of Petrology*, 46(4): 829–858.
- Zheng, Y.C., Hou, Z.Q., Li, W., Liang, W., Huang, K.X., Li, Q.Y., Sun, Q.Z., Fu, Q., and Zhang, S., 2012. Petrogenesis and geological implications of the Oligocene Chongmuda-Mingze adakite-like intrusions and their mafic enclaves, southern Tibet. *the Journal of Geology*, 120(6): 647–669.
- Zheng, Y.C., Hou, Z.Q., Gong, Y.L., Liang, W., Sun, Q.Z., Zhang, S., Fu, Q., Huang, K.X., Li, Q.Y., and Li, W., 2014. Petrogenesis of Cretaceous adakite-like intrusions of the Gangdese Plutonic Belt, southern Tibet: Implications for mid-ocean ridge subduction and crustal growth. *Lithos*, 190: 240–263.
- Zhu, D.C., Pan, G.T., Chung, S.L., Liao, Z.L., Wang, L.Q., and Li, G.M., 2008. SHRIMP Zircon Age and Geochemical Constraints on the Origin of Lower Jurassic Volcanic Rocks from the Yeba Formation, Southern Gangdese, South Tibet. *International Geology Review*, 50(5): 442–471.
- Zhu, D.C., Mo, X.X., Niu, Y.L., Zhao, Z.D., Wang, L.Q., Liu, Y.S., and Wu, F.Y., 2009. Geochemical investigation of Early Cretaceous igneous rocks along an east–west traverse throughout the central Lhasa Terrane, Tibet. *Chemical Geology*, 268(3–4): 298–312.
- Zhu, D.C., Mo, X.X., Zhao, Z.D., Niu, Y.L., Wang, L.Q., Chu, Q.H., Pan, G.T., Xu, J.F., and Zhou, C.Y., 2010. Presence of Permian extension- and arc-type magmatism in southern Tibet: Paleogeographic implications. *Geological Society of America Bulletin*, 122(7–8): 979–993.
- Zhu, D.C., Zhao, Z.D., Niu, Y.L., Mo, X.X., Chung, S.L., Hou, Z.Q., Wang, L.Q., and Wu, F.Y., 2011. The Lhasa Terrane: Record of a microcontinent and its histories of drift and growth. *Earth and Planetary Science Letters*, 301(1–2): 241–255.
- Zhu, D.C., Zhao, Z.D., Niu, Y.L., Dilek, Y., Hou, Z.Q., and Mo, X.X., 2013. The origin and pre-Cenozoic evolution of the Tibetan Plateau. *Gondwana Research*, 23(4): 1429–1454.

About the first author

XU Bo, is a PhD candidate from School of Earth Science and Mineral Resources, China University of Geosciences Beijing. He is now interested in the study on mineralogy, in situ analysis of various minerals and related ore deposits. E-mail: bo.xu@mail.com